Received: 31 May 2022 | Revised: 13 October 2022 | Accepted: 25 November 2022 | Published on: 2 March 2023

DOI: 10.1002/qj.4414

Quarterly Journal of the Royal Meteorological Society RMetS

RESEARCH ARTICLE

Implementation of a double moment cloud microphysics scheme in the UK met office regional numerical weather prediction model

Paul R. Field[1,2] | **Adrian Hill**[1] | **Ben Shipway**[1] | **Kalli Furtado**[1] | **Jonathan Wilkinson**[1] | **Annette Miltenberger**[3] | **Hamish Gordon**[2,4] | **Daniel P. Grosvenor**[2] | **Robin Stevens**[5] | **Kwinten Van Weverberg**[1,6]

[1]Met Office, Exeter, UK

[2]School of Earth and Environment, University of Leeds, Leeds, UK

[3]Institute for Atmospheric Physics, Johannes Gutenberg University, Mainz, Germany

[4]Department of Chemical Engineering and Center for Atmospheric Particle Studies, Carnegie Mellon University, Pennsylvania, Pittsburgh, USA

[5]Department of Chemistry, Université de Montréal, Montréal, Canada

[6]Department of Geography, Ghent University, Belgium

Correspondence
Paul R. Field, Met Office, Exeter, UK.
Email: paul.field@metoffice.gov.uk

Funding information
FP7 Coordination of Non-Community Research Programmes, Grant/Award Number: 603445; H2020 Environment, Grant/Award Number: 641727; NASA roses, Grant/Award Numbers: 80NSSC19K0949, 80NSSC21K1344; Natural Environment Research Council, Grant/Award Number: NE/L013584/1; Newton Fund, Grant/Award Number: CSSP

Abstract

Cloud microphysics parametrizations control the transfer of water between phases and hydrometeor species in numerical weather prediction and climate models. As a fundamental component of weather modelling systems cloud microphysics can determine the intensity and timing of precipitation, the extent and longevity of cloud cover and its impact on radiative balance, and directly influence near surface weather metrics such as temperature and wind. In this paper we introduce and demonstrate the performance of a double moment cloud microphysical scheme (CASIM: Cloud AeroSol Interacting Microphysics) in both midlatitude and tropical settings using the same model configuration. Comparisons are made against a control configuration using the current operational single moment cloud microphysics, and CASIM configurations that use fixed in-cloud droplet number or compute cloud droplet number concentration from the aerosol environment. We demonstrate that configuring CASIM as a single moment scheme results in precipitation rate histograms that match the operational single moment microphysics. In the midlatitude setting, results indicate that CASIM performs as well as the single moment microphysics configuration, but improves certain aspects of the surface precipitation field such as greater extent of light (<1 mm $\cdot$ hr^{-1}) rain around frontal precipitation features. In the tropical setting, CASIM outperforms the single moment cloud microphysics as evident from improved comparison with radar derived precipitation rates.

KEYWORDS

CASIM, double moment microphysics, NWP

1 | INTRODUCTION

Numerical weather prediction (NWP) is important for a wide range of applications (e.g., public weather service, defence, insurance, agriculture, commodity trading, sporting events) and underpins warning and downstream hazard systems. This motivates continuous improvement of the representation of physical processes related to extreme weather conditions. In atmospheric NWP models, both high-resolution kilometre-scale and coarser models, there are four components that control cloud formation on daily time-scales. These are (i) dynamics, (ii) mixing by a planetary boundary-layer representation, (iii) a cloud-fraction scheme that represents subgrid humidity fluctuations and handles condensation, and (iv) the cloud microphysics that represents formation of precipitation and associated sedimentation following condensation through warm, mixed-phase, and cold processes. In coarse models, convection also plays a large part in atmospheric mixing, and thus also plays a significant role in cloud and precipitation processes. Though radiation is important for fog and stratocumulus development, on longer time-scales radiative transfer becomes increasingly important to the cloud evolution through feedback on circulation.

Cloud microphysics representations in operational settings have slowly been increasing in complexity from simple prognosed condensate with diagnostic precipitation and temperature-dependent thermodynamic water phase (Senior and Mitchell, 1993) to the inclusion of prognostic rain (Lean *et al.*, 2008) and snow (Wilson and Ballard, 1999). The further addition of graupel can provide a way of linking lightning to microphysical processes (e.g., McCaul Jr. *et al.*, 2009). These efforts were largely accomplished with single-moment representations: only the mass mixing ratio of the hydrometeor was prognosed. In such a single-moment representation, the number concentration, which is required to estimate mean sizes and therefore microphysical process rates and sedimentation fluxes, is implicit in the assumptions made about the particle size distributions (PSDs) for each hydrometeor type. This approach has appeared to work well in the midlatitudes, where precipitation is dominated by ice processes that either melt to form rain or precipitate as snow (Field and Heymsfield, 2015). Indeed, the Met Office has kept the single-moment operational approach for nearly 25 years despite evidence suggesting that single-moment cloud microphysics does not adequately represent precipitation processes such as midlatitude convection (e.g., Milbrandt and Yau, 2006; Dawson *et al.*, 2010; Bryan and Morrison, 2012). In the Tropics, however, the performance of a single-moment scheme in the Met Office Unified Model (UM) has not been as skilful (Bush *et al.*, 2020). Over the past three decades a new wave of operational microphysics schemes have been developed and researched, which prognose the number concentration of hydrometeors along with the mass mixing ratios (e.g., Ferrier, 1994; Meyers *et al.*, 1997; Cohard and Pinty, 2000; Milbrandt and Yau, 2005a,b; Seifert and Beheng, 2006; Morrison and Gettelman, 2008; Thompson and Eidhammer, 2014; Vie *et al.*, 2016; Taufour *et al.*, 2018). These schemes can explore more combinations of mass and number, and hence mean size of the hydrometeor size distribution, than single-moment schemes can, which are generally locked into a fixed number or size. As well as prognosing number, other approaches have been suggested, such as a prognostic density for ice to capture the impact of riming (Mansell *et al.*, 2010; Morrison and Milbrandt, 2015) and prognostic shape information for ice based on growth characteristics (Hashino and Tripoli, 2007).

The initial requirement and drive for more complex bulk cloud microphysics representation, such as double-moment schemes was motivated by the recognition that indirect aerosol–cloud interactions are highly uncertain and poorly represented by single-moment schemes, which impedes the usefulness of climate predictions. Adopting double-moment cloud microphysics allows aerosol changes to directly feed into the microphysics and affect the cloud evolution, radiative response, and dynamical feedbacks. Moreover, double-moment cloud microphysics has been recommended to be used for cloud-resolving simulations as this tends to outperform the simpler single-moment representations in terms of precipitation, cloud structure, and feedback on atmospheric parameters (Morrison *et al.*, 2009; Igel *et al.*, 2015). For these reasons, many climate models (e.g., Lohmann *et al.*, 2007; Morrison and Gettelman, 2008) have taken the lead in operationally using double-moment microphysics ahead of NWP, whereas in operational NWP the use of double-moment schemes is much less common. For example, at the time of writing only two regional systems – the Canadian Global Environmental Multiscale (GEM) model and the US continental convection-permitting models RAP (Rapid Refresh) and HRRR (High-Resolution Rapid Refresh) – use multi-moment schemes operationally. For the GEM model, Milbrandt and Yau (2005a,b) scheme is employed, which was recently upgraded to Morrison and Milbrandt (2015) (Jouan *et al.*, 2020). For RAP and HRRR, the aerosol-aware cloud microphysics (Thompson and Eidhammer, 2014) scheme has double-moment cloud water, cloud ice, and rain and single-moment snow and graupel (Dowell *et al.*, 2022).

In this article, we introduce the coupling of the Cloud AeroSol Interacting Microphysics (CASIM) to the UK Met Office UM and demonstrate CASIM's performance in regional NWP. CASIM is implemented as a

double-moment, five species (cloud, rain, ice, snow, and graupel) microphysics scheme. Directly prognosing number concentration of cloud and ice particles brings the ability to predict those numbers from atmospheric aerosol acting as cloud condensation nuclei or ice nucleation particles. Such coupling to aerosol can go from simple mass-based diagnosis (e.g., Jones *et al.*, 1994) to depending on mass, number, and solubility characteristics for cloud condensation nuclei (Vogel *et al.*, 2009). Here, we will describe simple coupling of CASIM to mass-only aerosols, and briefly the coupling to a more complex aerosol representation (Mann *et al.*, 2010; Bellouin *et al.*, 2013; Walters *et al.*, 2019), with a more detailed description available in Gordon *et al.* (2018, 2020).

Recognising that weather prediction is a critical test of atmospheric models, this article describes a first step of integrating CASIM into the operational regional model of the UK Met Office. This nested model configuration is typically run with grid scales of 4 to 1 km operationally over domains in Europe, North America, Asia, Africa, and Australasia. Operationally dealing with this diverse range of environments has led to a bifurcation of configurations for midlatitudes and the Tropics. Ideally, recognising that a single representation of the appropriate physics should apply equally across the world, implementing improved physics should lead to closer unification of regional configurations.

In the next section the UM is briefly introduced; Section 3 then describes the datasets and modelling suites that have been employed to test CASIM. Section 4 steps through statistical verification results and demonstrates some illustrative cases, and Section 5 discusses the impact of the changes and concludes. Finally, the Appendix details much of the cloud microphysics description with further details of the process rates and assumptions for coupling to the UM.

2 | THE UNIFIED MODEL

The UK Met Office UM is used at a range of scales and geographical regions for climate and NWP. In this article, we show the model's performance for two different configurations: the operational United Kingdom Variable grid (UKV) configuration to assess midlatitude performance (Tang *et al.*, 2013) and a configuration based over Darwin, northern Australia, to assess tropical performance.

The simulations presented here employ a 1.5 km horizontal grid (which stretches at the edges to 4.5 km for the UKV tests (Bush *et al.*, 2020). There are 90 levels in the vertical stretched to 40 km (52 below 10 km, 33 below 4 km, 16 below 1 km). The time step is 60 s. Lateral boundary conditions are supplied at 1 hr intervals. For the UKV the boundary and initial conditions come from the operational global model, which at the time of writing uses N1280 resolution (~15 km grid spacing) and Global Atmosphere (GA) 7.0 science configuration (GA7.0; Walters *et al.*, 2019). For the Tropical, Darwin suite, the boundary and initial conditions come from European Centre for Medium-Range Weather Forecasts operational analyses.

The UM is non-hydrostatic and uses a semi-Lagrangian dynamical formulation (Cullen *et al.*, 1997; Davies *et al.*, 2005). For the regional simulations presented there is no parametrised convection. Vertical mixing due to turbulence is carried out by the scale-aware non-local one-dimensional boundary-layer scheme (Lock *et al.*, 2000; Boutle *et al.*, 2014) that uses profiles of potential temperature winds and humidity to determine the non-local mixing. The treatment of the radiative impact of cloud water and total ice and snow is handled by the radiation scheme (Manners *et al.*, 2018). Although the regional simulations are kilometre scale, the UM employs one of several cloud fraction schemes to represent subgrid humidity and carry out condensation of liquid.

The bimodal cloud fraction scheme used here (Van Weverberg *et al.*, 2021) diagnoses the subgrid cloudiness in each grid box from the large-scale model state, allowing for two modes of variability to coexist near sharp inversions. To do so, the scheme first identifies entrainment zones associated with these inversions. For grid boxes located in these entrainment zones, distinct moist and dry Gaussian modes are used to represent the subgrid conditions. The mean and width of the Gaussian modes, inferred from the turbulent characteristics, are then used to diagnose the liquid water content and liquid cloud fraction, taking into account competition of water vapour between ice and liquid, following Field *et al.* (2014). Ice and snow water content are prognosed by the microphysics scheme. The frozen cloud fraction is obtained by applying the diagnostic relation between cloud water content and cloud fraction to the combined cloud ice and snow mass, assuming Gaussian subgrid variability with variances inferred from the turbulent properties and allowing for bimodal distributions near entrainment zones. A single frozen fraction is applied to the ice and snow species.

The current operational UM cloud microphysics is a single-moment, three-phase representation. For the liquid phase there are prognostic variables for cloud water and rain mixing ratio. For ice there is a prognostic variable for snow mass mixing ratio that represents all ice in the grid box. Production of cloud water is through condensation and from sedimentation from above. Loss occurs through droplet settling, autoconversion of droplets to rain, freezing of droplets by ice nucleation, and riming. Production of rain mixing ratio is via autoconversion, accretion, and melting of ice. Loss of rain mixing ratio is

from evaporation, capture by ice (which freezes rain), and homogeneous ice nucleation. Sedimentation can lead to loss or gain of rain. Ice mixing ratio production is from diffusional growth, capture of rain, and riming. Loss of ice mixing ratio comes from sublimation and melting. Sedimentation acts on the ice mixing ratio. The basic formulation is described in Wilson and Ballard (1999).

The new cloud microphysical scheme we introduce here is the Cloud AeroSol Interacting Microphysics (CASIM). CASIM is an open-source, configurable, multimoment bulk microphysics scheme, which has been developed to represent cloud microphysics processes and aerosol–cloud interactions across spatial and temporal scales. CASIM has been designed to easily interface with parent atmospheric models of differing dynamic complexity – for example, kinematic, large-eddy simulation, NWP, and climate model – enabling easy application to research and operations. As such, CASIM is the long-term replacement for the present operational scheme in the Met Office UM and a focus for consolidation of cloud microphysical and aerosol–cloud research and modelling effort in the Met Office.

CASIM represents cloud by using five hydrometeor species: cloud liquid, rain, ice, snow, and graupel. Since CASIM is multimoment, these species can all be specified by one prognostic moment (mass mixing ratio) or two moments (mass mixing ratios and species number concentration). In addition, rain, snow, and graupel can be represented with three prognostic moments (mass mixing ratios, number concentration, and a third moment, such as one that can be related physically to radar reflectivity). CASIM has been developed in such a way as to make it configurable so that the user can define the number of cloud species and the associated number of moments. For instance, CASIM can be used in single-moment mass mixing ratio mode (Furtado *et al.*, 2016) where details of the PSD, such as shape and number concentration, are assumed or diagnosed from the mass mixing ratio. CASIM also represents aerosol activation, ice nucleation processes, and in-cloud mechanical processing of aerosol. In brief, if CASIM is configured to represent aerosol processing, then, once aerosol is activated to cloud droplets or nucleated to ice particles, the aerosol will be transferred into an activated in-cloud prognostic, which is treated as another cloud prognostic (e.g., Ghan and Easter, 2006). This permits the transport of in-cloud aerosol by cloud dynamics and sedimentation, as well as allowing the growth of aerosol through collision–coalescence.

CASIM was first introduced by Shipway and Hill (2012) in the Kinematic Driver model and has since been further researched and developed in that model (Hill *et al.*, 2015; Miltenberger *et al.*, 2020), the Met Office–NERC cloud (MONC) model (e.g., Dearden *et al.*, 2018; Poku *et al.*, 2021; Hawker *et al.* 2021), and various bespoke configurations of the UM (e.g., Grosvenor *et al.*, 2017; Miltenberger *et al.*, 2018; Stevens *et al.*, 2018), which have aerosol–cloud interactions with and without in-cloud mechanical processing. In this work, we present the first time that CASIM has been fully coupled to the UM for operational testing and implementation as part of the Met Office Regional Atmosphere and Land (RAL) process. Though CASIM includes the configurable complexity at the heart of its design, the implementation and testing of CASIM for operational application focuses on the double-moment configuration, CASIM-2M, in which mass and number concentration mixing ratios are prognosed for cloud droplets (Note that configurations using both aerosol derived and prescribed in-cloud droplet number concentration are demonstrated), rain, cloud ice, snow, and graupel. The PSDs for each are represented by a generalised gamma function with fixed shape parameter. The parameters describing the PSDs and particle characteristics, as well as a brief description of the processes can be found in the Appendix.

We show some single-moment CASIM results for comparison, and for this configuration the default rain and graupel size distributions are replaced with the parametrisations used in the Wilson–Ballard (WB) scheme. For ice and snow, we made the scheme similar to WB single-ice-category microphysics by following the method in Furtado *et al.* (2016). This involves (a) removing the second ice category, so that there is only one hydrometeor species for ice and snow combined, (b) using the WB mass–diameter relation for the particles of the single ice–snow species (as is used for CASIM-2M snow), and (c) modifying the parametrisation of mass-weighted mean fall speed to follow the WB scheme.

3 | DATASETS USED IN COMPARISONS

For acceptance for the RAL science configuration in the Met Office, it is necessary for any model changes to undergo extensive, detailed testing and analysis against observations and associated verification statistics to understand the impact of the change across a wide range of environments. In this section, we briefly describe the test case-study suites and the verification datasets, as well as additional datasets used to assess the model performance.

3.1 | Case-study suites

As first defined in Bush *et al.* (2020), general RAL testing is based on two extensive sets of case studies performed with the UM. One, the UKV suite, is situated over the UK and

is based on the operational model set-up, UKV. This suite includes a set of 124 days spread throughout July 2017 to September 2019 that cover a range of different weather regimes; for example, fog, stratocumulus, summertime convective storms, and frontal conditions. All simulations in this suite are 36 hr in length and use a stretch grid that extends the grid from 1.5 km grid resolution in the inner region to 4 km at the extremes (see Bush *et al.*, 2020). The UKV suite is initialised from the 12Z analysis and boundary conditions derived from the Met Office operational global model (GA7.0, Walters *et al.*, 2017). The other case study suite, the Darwin suite, is a contiguous set of tropical simulations, centred over Darwin, which run from January 21 to March 17, 2017. Each simulation in the Darwin suite is 36 hr long, the grid resolution is 1.5 km, and the runs are initialised using European Centre for Medium-Range Weather Forecasts reanalysis (Hersbach *et al.*, 2020) at 0000 UTC and 1200 UTC each day to give 112 simulations. The spin-up periods for the UKV and Darwin suites are approximately 6 hr and 10 hr respectively.

The tropical case-study suite dates were chosen by the Regional Model Evaluation and Development (RMED) in collaboration with the Bureau of Meteorology in Australia to cover a range of weather conditions. The intention was to choose a period that contained tropical storms, a tropical cyclone and squall lines. Between these events there were dry periods with clear skies or fair-weather cumulus. The Darwin cases use start dumps derived from 1200 UTC and 0000 UTC analyses. This is because the analysis can be biased by shortcomings in the diurnal behaviour of parametrised convection in the global model used to form the analysis.

In this work, the control runs are provided by a bimodal cloud fraction scheme set-up that uses the WB microphysics (Van Weverberg *et al.*, 2021). To test and understand the influence of CASIM-2M, we present two variations of the UKV and Darwin suite experiments to explore (i) differences associated with changing the cloud microphysics to CASIM with prescribed cloud droplet number and (ii) differences in diagnosing a cloud droplet number concentration based on aerosol (Table 1).

3.2 | Verification datasets

Verification of the various configurations' (Table A1) performances is based on methods outlined in Bush *et al.* (2020). In brief, the skill of the kilometre-scale regional simulation is assessed using the standard RMED "toolbox" for the RAL configuration assessment. Standard synoptic (WMO Guide to the Global Observing System) observations (including screen level temperature, relative humidity, 10 m wind, cloud cover, and rain-gauge) and remote sensing (radar) are compared with the model forecasts to assess the model skill. In addition to bias and root-mean-square error (RMSE), we verify model configurations using histograms of the relative frequency of mean surface precipitation versus radar observations (Harrison *et al.*, 2000), which are also generated from the RMED "toolbox". A detailed description of the tools and approach used for assessing the skill of kilometre-scale-resolution regional models used for NWP is given in Bush *et al.* (2020) and references therein.

3.3 | Radar reflectivity

In addition to the verification tools in the "toolbox", we also use two-dimensional normalised histograms of radar reflectivity (dBZ) against height – that is, contoured frequency by altitude diagrams (CFADs - Yuter and Houze, 1995) – to assess CASIM. For the UK these make use of the three-dimensional 1 km radar composite produced from the UK radar network (Scovell and Al-Sakka, 2016) with 500 m vertical spacing and a minimum sensitivity of +0 dBZ. Stein *et al.* (2020) recently showed good agreement between the UK network composite and the Chilbolton research radar for reflectivities in the range 0–30 dBZ, with greater reflectivities underreported in convective cases.

TABLE 1 Model configurations

Model configuration	Comment
WB	Midlatitude configuration using WB microphysics and bimodal cloud fraction scheme
CASIM-2M	Same as WB but replace microphysics with the double-moment CASIM microphysics. This uses a prescribed in-cloud number of droplets (this is the candidate operational RAL3 configuration)
CASIM-2M murk/arcl	Same as CASIM-2M but this uses a droplet number concentration derived from MURK prognostic aerosol over the UK or ARCL climatology elsewhere. These aerosols are simple single-moment mass-only representations (see Appendix)
CASIM-1M	Same as CASIM-2M but uses the cloud microphysics in single-moment mass-only mode

Note: Only the microphysics is changed between configurations. All other model settings are the same for each configuration.
Abbreviations: CASIM, cloud aeroSol interacting microphysics; WB, Wilson–Ballard.

For Darwin, the c-band polarimetric radar (CPOL) radar provides a three-dimensional volume with 2.5 km horizontal and 500 m vertical spacing out to a radius of ~200 km from the radar (Louf *et al.*, 2019). For 2017, the CPOL radar sensitivity is +15 dBZ (C. Franklin, personal communication). For both radars' $T + 18$, 24, 30, 36 hr datasets, instantaneous output from the model was compared with six-hourly data from the radars.

For both regions the normalisation at each height level includes values below the sensitivity of the radars. To compare against the model, the same forward operator using a simple Rayleigh scattering assumption using either the prognosed or diagnosed PSD settings was used for all of the configurations.

3.4 | Satellite broadband fluxes

Finally, we assessed model configurations (Table A2) using the top of the atmosphere (TOA) broadband fluxes done in the same way for each of the model configurations (Manners *et al.*, 2018) to appraise the overall impact on outgoing radiation. This assessment was performed using the synoptic TOA hourly 1° gridded fluxes at $T + 24$ hr into the forecast (27 hr for Darwin for local midday). This is compared with the Clouds and Earth's Radiant Energy System product that combines Moderate Resolution Imaging Spectroradiometer level 3 gridded data with geostationary data to obtain a traceable calibrated dataset Doelling *et al.*, (2013). Edition 4.1 (2017–2019) estimates of long-wave and short-wave broadband flux were used for this analysis.

4 | RESULTS

4.1 | Near-surface performance

Figure 1 shows the bias and RMSE between near-surface synoptic observations and the model predictions at increasing forecast range. The UKV forecasts are all initialised at 1200 UTC, so a 24 hr forecast range ($T + 24$) is at local midday. For 1.5 m temperature, 1.5 m relative humidity and 10 m wind the three configurations using the bimodal cloud-fraction scheme (CASIM-2M, CASIM-2M-murk, WB) all exhibit similar bias, with some indication that WB has a small (0.05 K) warm offset relative to the CASIM-2M configurations. Similarly, the RMSEs are comparable for these three configurations. For the surface observed cloud cover, the mean bias and RMSE of the CASIM-2M configurations (CASIM-2M, CASIM-2M-murk) improve upon the WB configuration.

Figure 2 shows the bias and RMSE as a function of forecast range offset by initialisation time for the Darwin domain. Because the Darwin trials were carried out using forecasts initialised at 0000 UTC and 1200 UTC, the 1200 UTC results are offset by 12 hr so that any systematic diurnal errors can be seen. For Darwin, $T + 27$ is approximately local midday. Both CASIM-2M configurations (CASIM-2M, CASIM-2M-arcl) show improved bias relative to the non-CASIM configuration (WB) for 1.5 m temperature and relative humidity away from local noon. Relative to the WB configuration, the RMSE for temperature and relative humidity is improved for CASIM-2M in the local morning, but worse in the local afternoon. Cloud cover is improved, with CASIM-2M-arcl exhibiting the least bias for cloud cover. The 10 m wind performance is similar for all configurations. For the CASIM-2M-arcl configuration the RMSE for cloud cover is improved in the local morning but does show degradation for the local mid-afternoon point (30 hr), although the 1200 UTC initialised forecast has a similar RMSE to the other configurations. For the 10 m wind, the WB configuration has consistently the least RMSE.

Taking the results for both the tropical and midlatitude settings together, the temperature and relative humidity biases are improved or similar for the CASIM-2M configurations relative to the WB configuration. Differences between the CASIM-2M configuration using a prescribed activated number or using MURK or ARCL are generally smaller than differences between the CASIM-2M and non-CASIM configurations with the exception of the Darwin cloud cover. The cloud cover biases are improved for the CASIM-2M configurations in the UKV with aerosol-based CASIM-2M-arcl having reduced bias relative to the CASIM-2M configuration in the Darwin tests. For the wind, all of the configurations are similar to each other.

4.2 | Precipitation

Precipitation bias (millimetres of precipitation accumulation in 1 hr) relative to rain-gauges for different grid-averaging of the model output (not shown) indicates for the UKV test that whereas the WB configuration hovers around 0.01 mm · hr^{-1} the CASIM-2M configurations have a positive bias of 0.01–0.02 mm · hr^{-1}. The Darwin trial indicates that biases from all configurations are comparable, with a bias magnitude of less than 1 mm · hr^{-1}. The UK radar network derived precipitation rate normalised histogram (Figure 3) shows that for precipitation rates below 1 mm · hr^{-1} the CASIM-2M configurations agree better with the radar predicting greater frequencies of occurrence of light rain-rates than the WB configuration using the operational microphysics. For comparison with the Darwin radar the precipitation rates derived

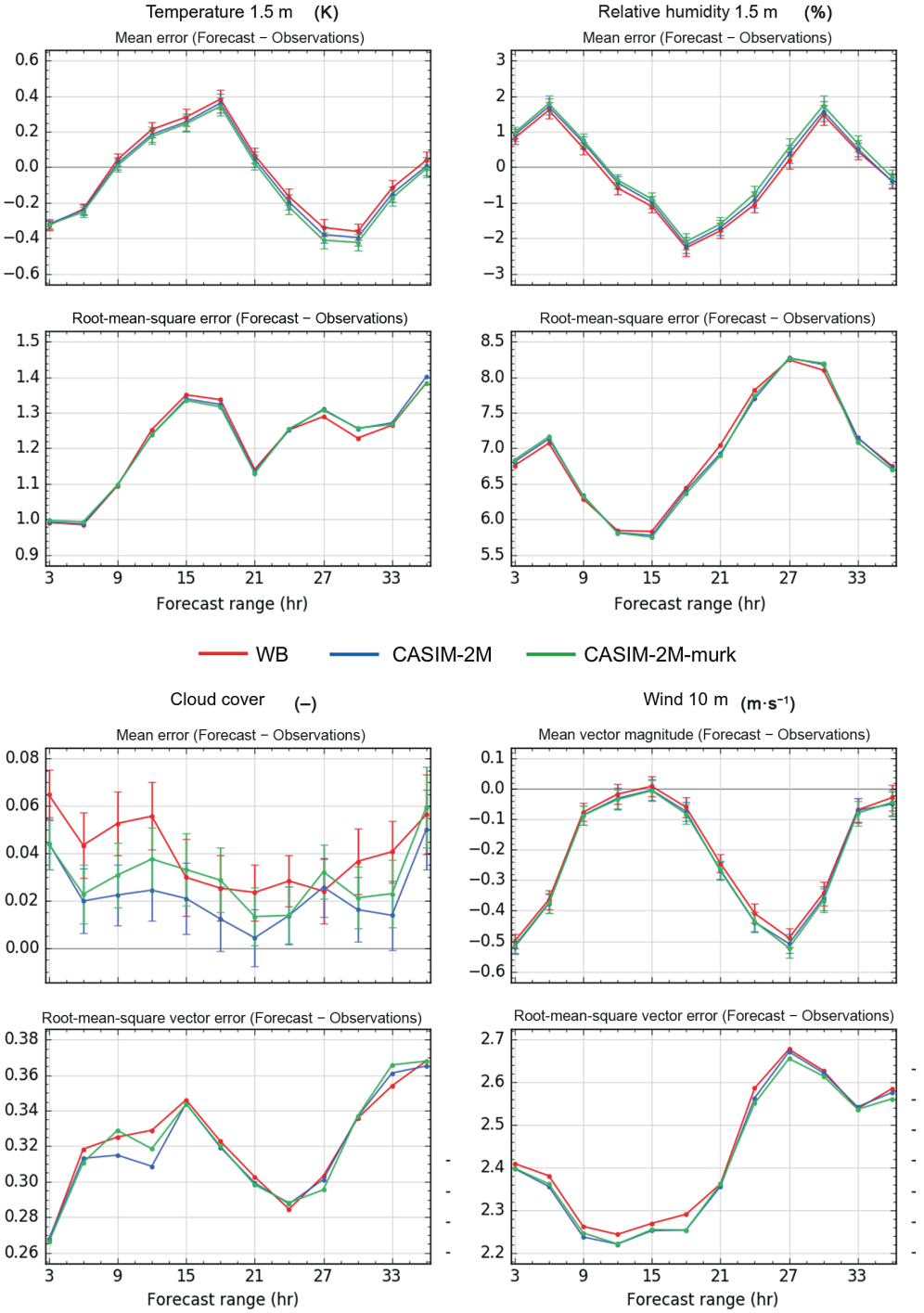

FIGURE 1 United Kingdom Variable grid case-study suite bias and root-mean-square error between near-surface synoptic observations of temperature, humidity, winds, and cloud cover and the model predictions at increasing forecast range. CASIM: Cloud AeroSol Interacting Microphysics; WB: Wilson–Ballard

from a single-moment CASIM configuration, CASIM-1M, have also been included for discussion. Comparison to the Darwin radar derived precipitation rates (Figure 4) shows that the CASIM-2M and CASIM-2M-arcl configurations have a higher frequency of occurrence of lighter precipitation rates than the single-moment cloud microphysics configurations (CASIM-1M and WB), which is in better agreement to the radar for precipitation rates below 4 mm · hr^{-1}. The largest differences occur for precipitation rates in excess of 20 mm · hr^{-1}. For these higher rain-rates the single-moment configurations exhibit greater frequencies of occurrence than the radar and CASIM-2M configurations indicate. For 40 mm · hr^{-1} precipitation rates the single-moment configurations are indicating 10 × greater frequency than the radar suggest, whereas the double-moment CASIM configurations are within a factor of 2 or better.

In the UK and Darwin trials, the CASIM-2M configurations agree better with the radar-derived precipitation rates. The CASIM-2M and CASIM-2M-murk/arcl

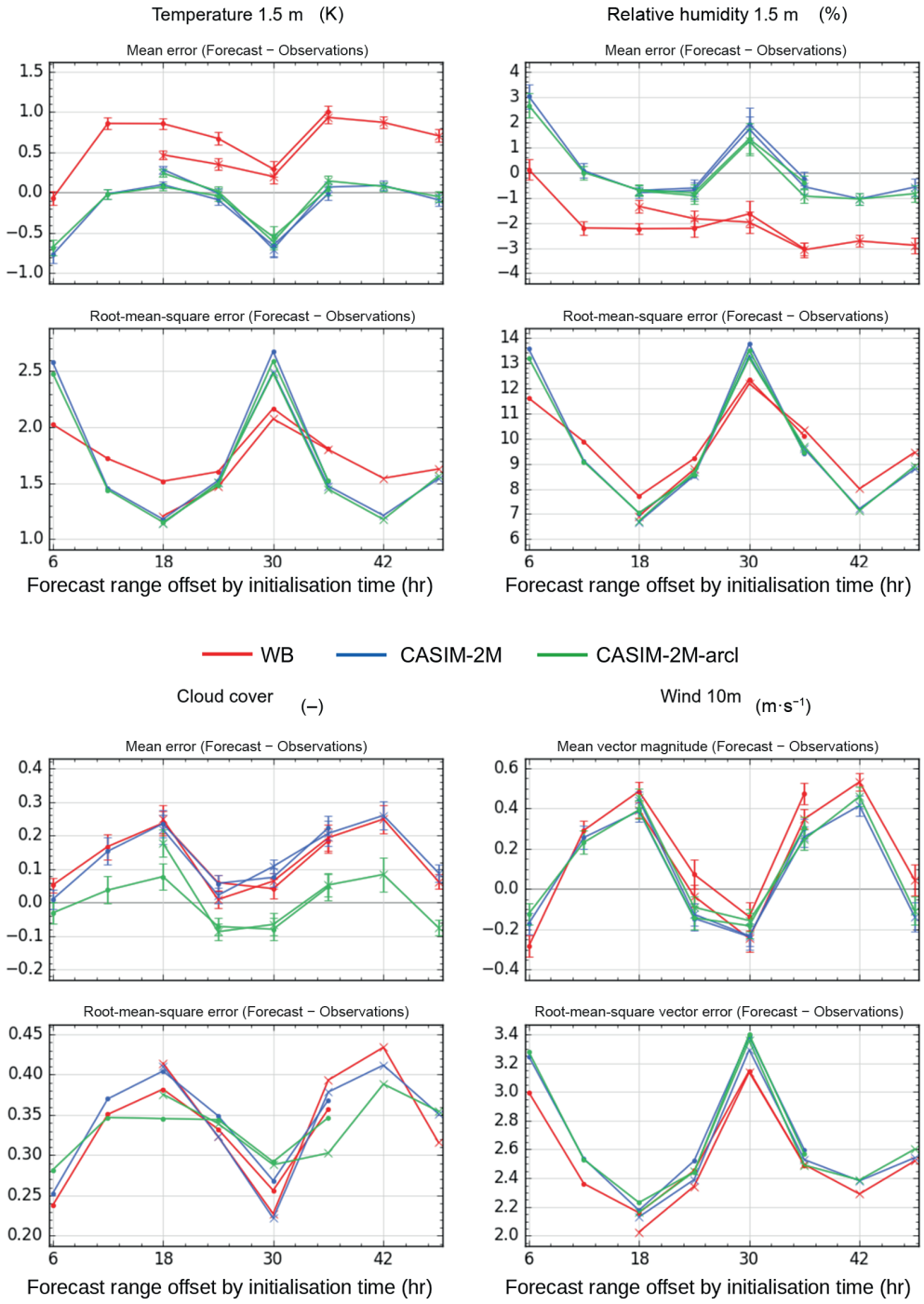

FIGURE 2 Darwin case-study suite bias and root-mean-square error between near-surface synoptic observations of temperature, humidity, winds, and cloud cover and the model predictions at increasing forecast range offset by initialisation time. The two lines show the results for simulations initialised at 0000 UTC (6–33) and 1200 UTC (18–45). CASIM: Cloud AeroSol Interacting Microphysics; WB: Wilson–Ballard

configurations produce greater frequencies of occurrence of lower precipitation rates (<2–4 mm · hr^{-1}) and lower frequencies of occurrence of large precipitation rates (>4–10 mm · hr^{-1}) than the single-moment cloud microphysics configurations (WB, CASIM-1M). However, against rain-gauge for the UK there is still a slight (<0.02 mm · hr^{-1}) positive bias that may be possible to correct in future configurations through modifications to the microphysics process rates that have less well constrained parameter settings and/or formulations (e.g., snow aggregation rate, rain coalescence rate, autoconversion rates).

4.3 | Radar CFADs

For the UKV the radar observations (Figure 5) show a broad triangular and evenly distributed two-dimensional histogram with a minimum between 2 and 4 km below 5 dBZ. WB has a maximum close to 5 km and 0 dBZ with a ridge extending towards 20 dBZ at the surface. Both CASIM-2M configurations are similar to each other and have a more pronounced ridge than the observations, stretching down from 6 km at 0 dBZ towards 20 dBZ at the surface and fill in the lower level (<2 km, <20 dBZ)

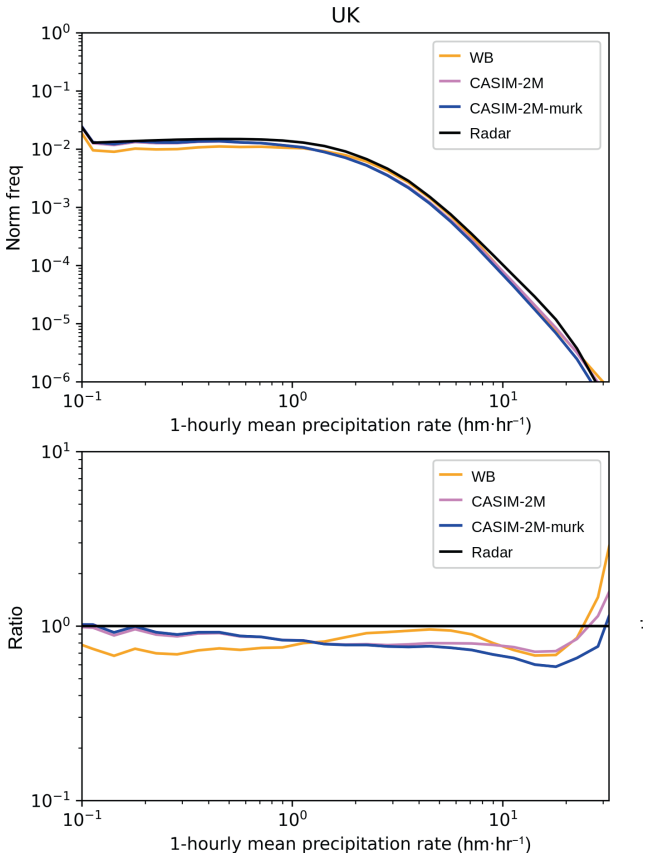

FIGURE 3 United Kingdom Variable grid case-study histograms of precipitation rate for the models and the radar-derived surface precipitation rate (top) and ratio of models to radar precipitation rate (bottom). Only bins with greater than 30 observations are shown. CASIM: Cloud AeroSol Interacting Microphysics; WB: Wilson–Ballard

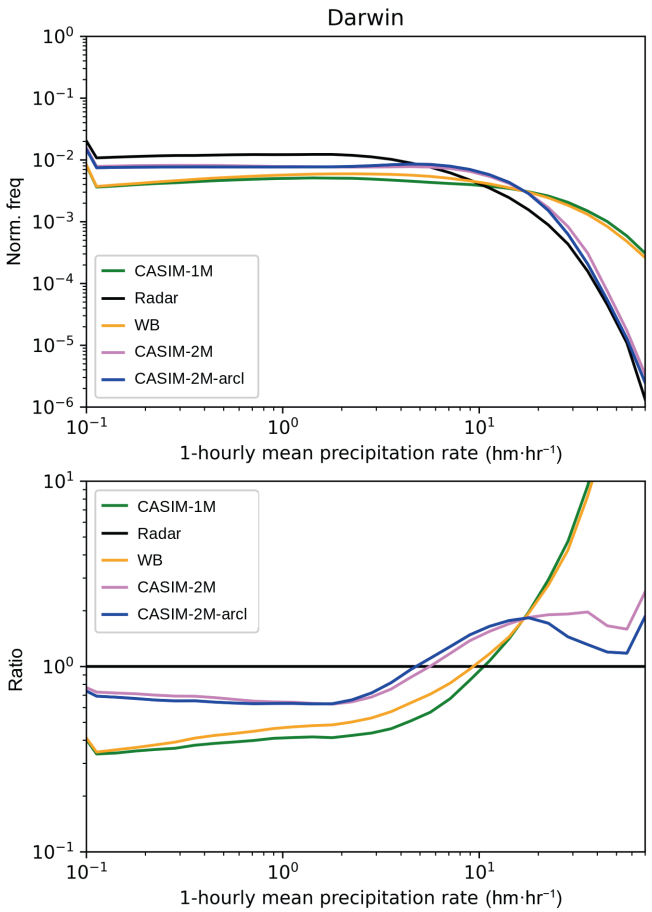

FIGURE 4 Darwin case-study histograms of precipitation rate for the models and the radar-derived surface precipitation rate (top) and ratio of models to radar precipitation rate (bottom). Only bins with greater than 30 observations are shown. CASIM: Cloud AeroSol Interacting Microphysics; WB: Wilson–Ballard

region of the CFAD more similar to the observations than WB. However, the CASIM-2M configuration does exhibit a local maximum near the surface between 15 and 20 dBZ that is not evident in the observations and is less obvious in CASIM-2M-murk.

The Darwin radar observations (Figure 6) show a triangular distribution from 5 km (approximate altitude of the freezing level), 35 dBZ to 10 km, 0 dBZ with a rectangular distribution below 5 km to the surface. For reflectivities <25 dBZ the frequency of occurrence decreases downwards from 5 km to the surface, and the frequency of occurrence decreases monotonically with increasing reflectivity at all heights. The WB configuration has a maximum close to 15 dBZ and 7 km, but there is a distinct discontinuity below 5 km and the impression of a broad ridge extending from 5 km, 20 dBZ to 0 km, 30 dBZ. For CASIM-2M the maximum is broader than the observations suggest and is at 6–7 km, 15–20 dBZ. The frequencies of occurrence are decreasing monotonically with increasing reflectivity below 5 km. There is an inverted triangular distribution behaviour below 5 km that is not present in the observations. The pattern of the CFAD for CASIM-2M-arcl is similar to CASIM-2M but is broader in terms of reflectivity values and extends to higher in the atmosphere than CASIM-2M.

4.4 | Broadband fluxes

Figure 7 shows histograms of observed and forecast (T + 24 hr) outgoing short-wave and long-wave radiation at the TOA regridded onto the Clouds and Earth's Radiant Energy System 1°-resolution data for the UKV domain. These histograms contain 120 scenes and include cloudy and clear-sky pixels. The observations show high frequencies of lower flux pixels for short wave that reduce in frequency towards the greater fluxes. All configurations perform similarly, matching the observations for fluxes below 450 W · m^{-2}. Above 450 W · m^{-2} all of the configurations

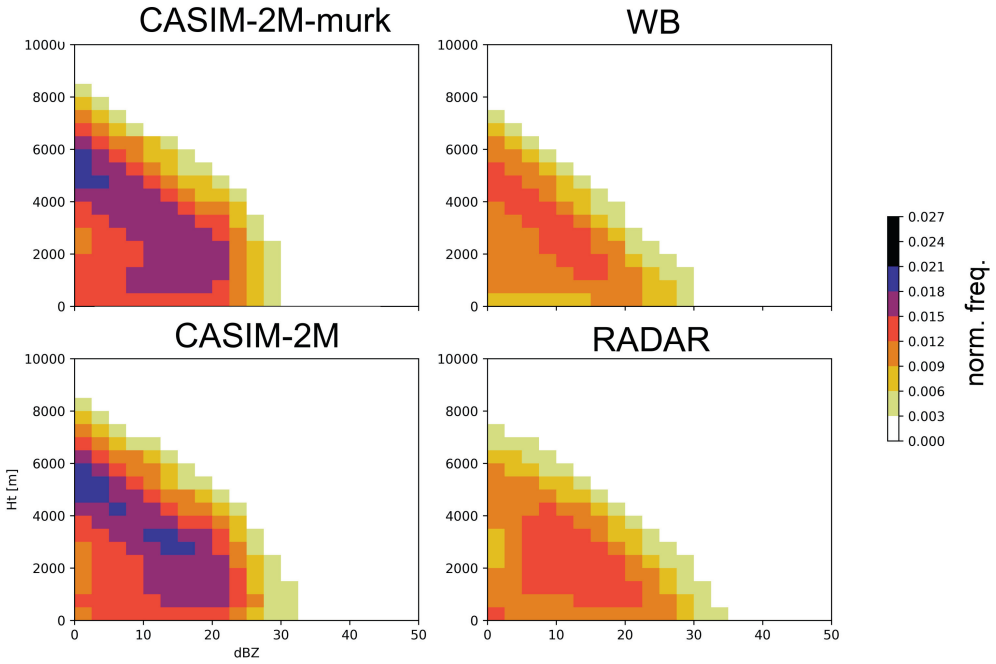

FIGURE 5 United Kingdom Variable grid two-dimensional normalised histograms (contoured frequency by altitude diagrams) of radar reflectivity and height. The normalisation includes values <0 dBZ. CASIM: Cloud AeroSol Interacting Microphysics; WB: Wilson–Ballard

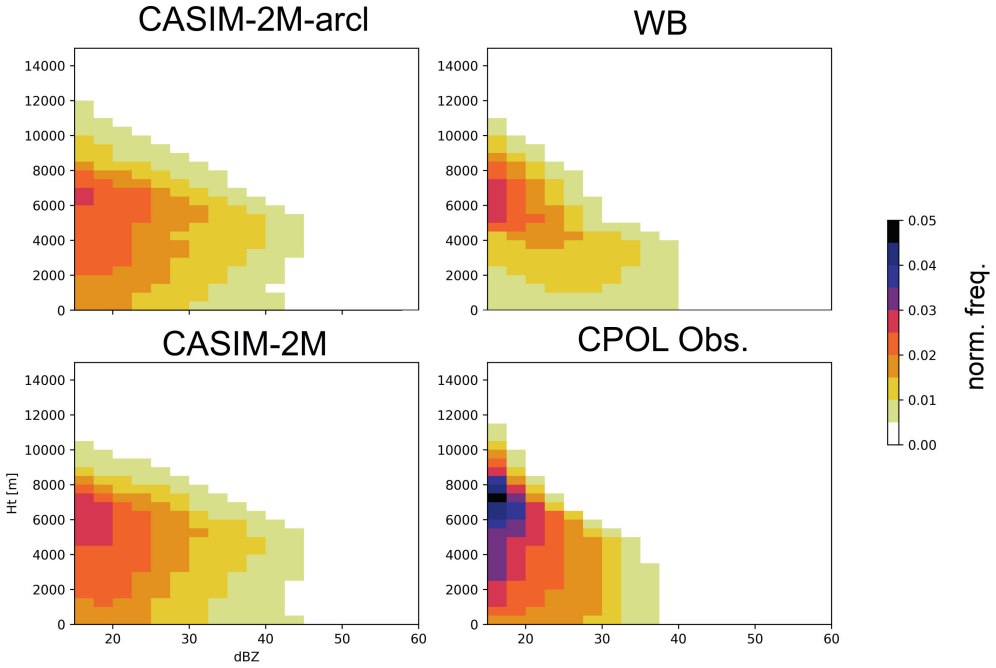

FIGURE 6 Darwin two-dimensional normalised histograms (contoured frequency by altitude diagrams) of radar reflectivity and height. Results are from a subset of days (February 1–20, 2017). Model output and the c-band polarimetric radar (CPOL) radar output are shown. The normalisation includes values <15 dBZ. CASIM: Cloud AeroSol Interacting Microphysics; WB: Wilson–Ballard

overestimate the frequency for fluxes (by a factor of ~2 between 600 and 700 $W \cdot m^{-2}$).

For the long-wave histogram, the histogram ramps up approximately linearly from the low flux end (100–150 $W \cdot m^{-2}$) that represents the emission from high, cold clouds, through a shoulder (~190 $W \cdot m^{-2}$) to a peak around 240 $W \cdot m^{-2}$ before rapidly falling off to values representative of low-level clouds (280 $W \cdot m^{-2}$). At the high flux end, the CASIM-2M and WB configurations are within 10% of the observations between 225 and 280 $W \cdot m^{-2}$. For the low flux end of the long-wave histogram, both CASIM-2M configurations overestimate the frequency for fluxes below 160 $W \cdot m^{-2}$ but underestimate the frequency of the shoulder feature (160–190 $W \cdot m^{-2}$). WB provides better agreement with observations relative to CASIM-2M for fluxes smaller than 190 $W \cdot m^{-2}$.

For Darwin, broadband TOA outgoing fluxes are shown in Figure 8 for $T + 27$ hr of the 0000 UTC run for each day and so represents 60 scenes. Again, the model output is regridded onto the 1° satellite data and contain

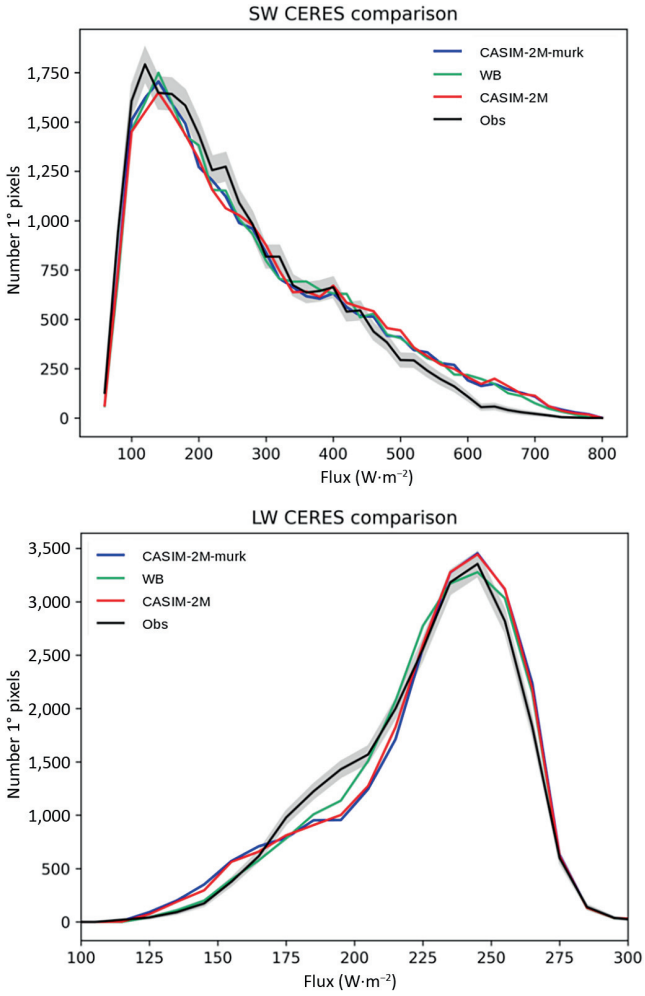

FIGURE 7 United Kingdom Variable grid area top-of-atmosphere outgoing broadband fluxes for short wave (SW; top) and long wave (LW; bottom). The shading represents ±2× Poisson uncertainty. CASIM: Cloud AeroSol Interacting Microphysics; CERES: Clouds and Earth's Radiant Energy System; WB: Wilson–Ballard

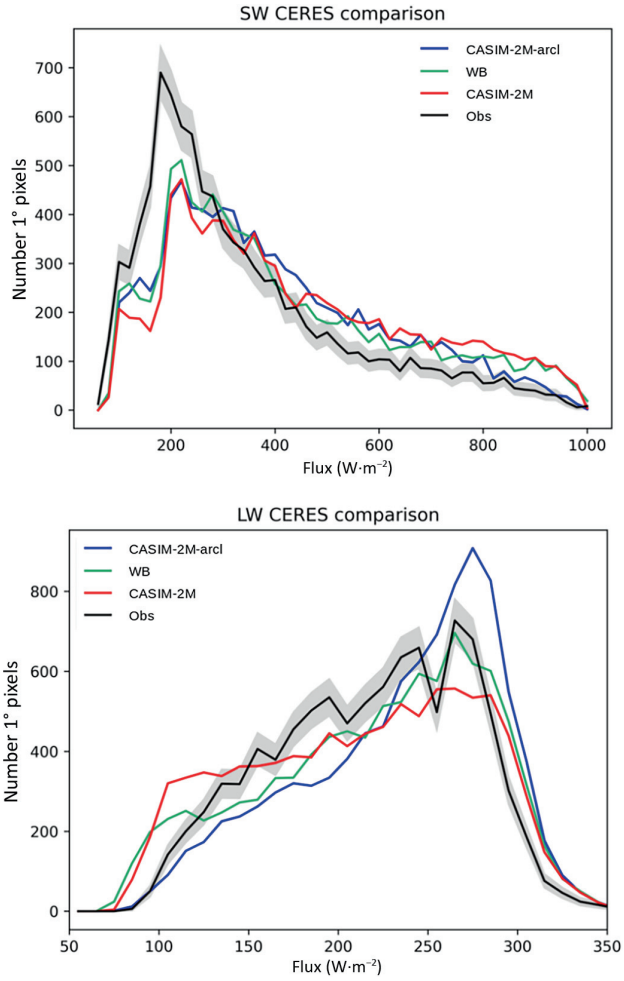

FIGURE 8 Darwin area top-of-atmosphere outgoing broadband fluxes for short wave (SW; top) and long wave (LW; bottom). The shading represents ±2× Poisson uncertainty. CASIM: Cloud AeroSol Interacting Microphysics; CERES: Clouds and Earth's Radiant Energy System; WB: Wilson–Ballard

cloudy and clear-sky pixels. For the short-wave comparison the observations show a mode in the frequency of the low flux values (200 W · m^{-2}) with a steady decrease towards the larger fluxes (bright pixels). WB overestimates the brightest pixels (>800 W · m^{-2}) but captures the behaviour of the observations at the low flux end of the distribution (~100 W · m^{-2}, 300–800 W · m^{-2}) yet underestimates the frequency between 150 and 300 W · m^{-2} relative to the observations. CASIM-2M-arcl captures the high-end tail (>800 W · m^{-2}) falling within the uncertainty envelope but overestimates the frequency of occurrence at intermediate fluxes (400–700 W · m^{-2}) and underestimates the frequency of occurrence for fluxes below 400 W · m^{-2}. CASIM-2M follows the CASIM-2M-arcl histogram apart for fluxes in the range 700–900 W · m^{-2}, where it overpredicts the bright flux end of the distribution.

For the long wave, the high flux shoulder of the WB configuration is within 10 W · m^{-2} at the high flux end but overestimates the frequency of occurrence of the low end fluxes (<100 W · m^{-2}). For the intermediate fluxes (150–200 W · m^{-2}) the WB configuration is on the lower edge or just below the observational uncertainty envelope. The CASIM-2M configuration has a flatter response across the flux range than WB, leading to an underestimate of the frequency of occurrence relative to observations for high fluxes. In contrast, CASIM-2M-arcl exhibits a pronounced peak at 275 W · m^{-2} and then has lower frequencies of occurrence than CASIM-2M, WB, and the observations for fluxes <225 W · m^{-2}. These biases in the long wave suggest that CASIM-2M and WB are overpredicting the coverage or altitude of cirrus cloud relative to observations. In contrast, CASIM-2M-arcl seems to be underestimating the coverage and or altitude of the cirrus cloud relative to observations.

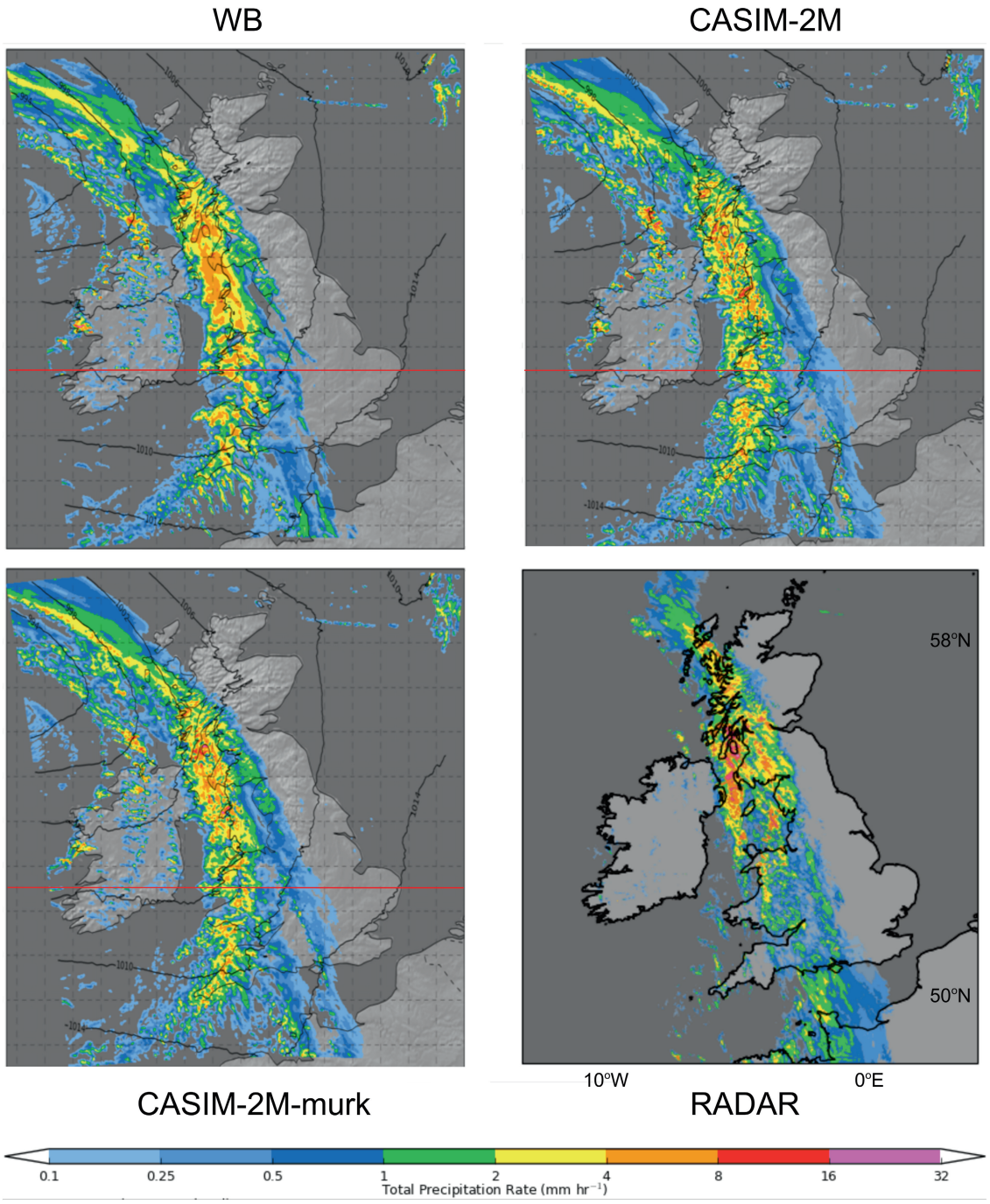

FIGURE 9 United Kingdom Variable grid frontal example showing $T + 12$ hr model precipitation rate simulations for Wilson–Ballard (WB), Cloud AeroSol Interacting Microphysics (CASIM)-2M, and CASIM-2M-murk, valid at 0000 UTC on March 27, 2018, along with the UK radar-network-derived precipitation rate at the same time. The red line indicates the location of the cross-sections. The solid contour lines are mean sea level pressure (mb).

4.5 | UK frontal example

Given the statistical result of the higher frequencies of lighter precipitation rates it is useful to examine what that looks like in a typical midlatitude frontal weather situation (0000 UTC, March 27, 2018). Precipitation rates for the four configurations (Figure 9) show similar gross structures across the domain at $T + 12$ highlighting a front running through Brittany to the Western Isles of Scotland. Closer inspection shows that when looking west to east across Wales into the Midlands it can be seen that whereas the WB bimodal configuration produces some lighter precipitation ($<2\,\text{mm} \cdot \text{hr}^{-1}$) ahead of the main frontal rain, the CASIM-2M and CASIM-2M-murk configurations

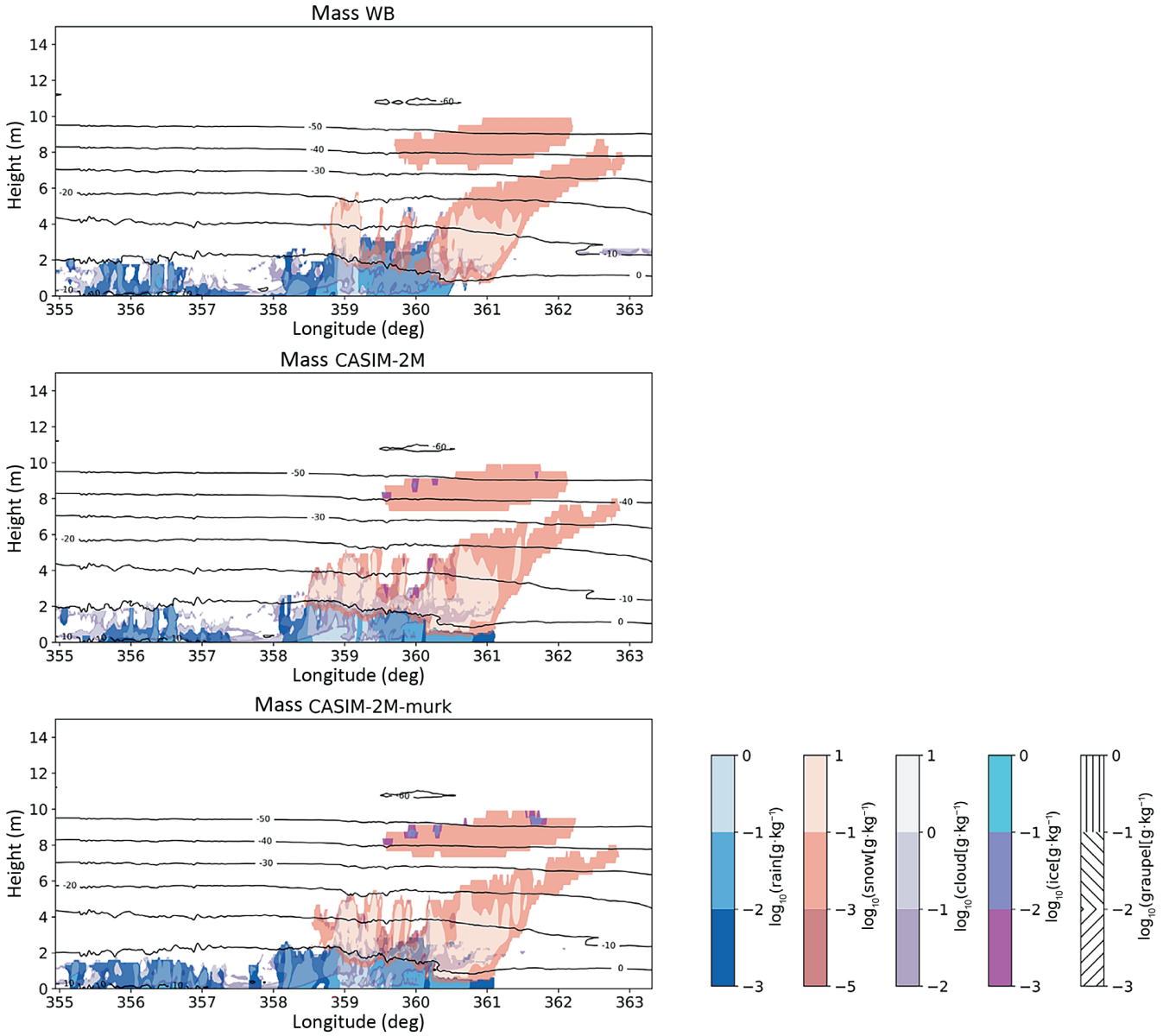

FIGURE 10 Cross-sections for March 27, 2018, 0000 UTC from the United Kingdom Variable grid Cloud AeroSol Interacting Microphysics (CASIM)-2M, CASIM-2M-murk, and Wilson–Ballard (WB) configurations at $T + 12$. Gridbox-mean mass mixing ratios are shown

extend these lower precipitation rates further and make the frontal rain into a more coherent structure than the WB configuration. For the CASIM-2M configurations, the more widespread lighter precipitation bridges the islands of more intense precipitation.

For illustrative purposes we have included model cross-sections of grid-box-averaged values and recognise that these are single cross-sections for a single case. Looking at model-to-model differences in an east–west cross-section through central Wales (Figure 10) shows all configurations with the snow extending up the frontal slope (360–362° rotated longitude), with a detached cirrus sheet at −35 to −55°C and post-frontal convection (<360° rotated longitude).

A clear difference between the CASIM-2M and non-CASIM configurations is the lack of lighter precipitation below the snow cloud (360.5–361° rotated longitude), explaining the reduced occurrence of this lighter precipitation on the area maps (Figure 9). Going from WB to CASIM-2M leads to some evidence of ice ($> 1 \times 10^{-3}$ g · kg^{-1}) being present in the upper-level cirrus deck and the deeper post-frontal (359–360°) convection appears narrower. And, as mentioned earlier, precipitation below the frontal snow cloud (360–361° rotated longitude)

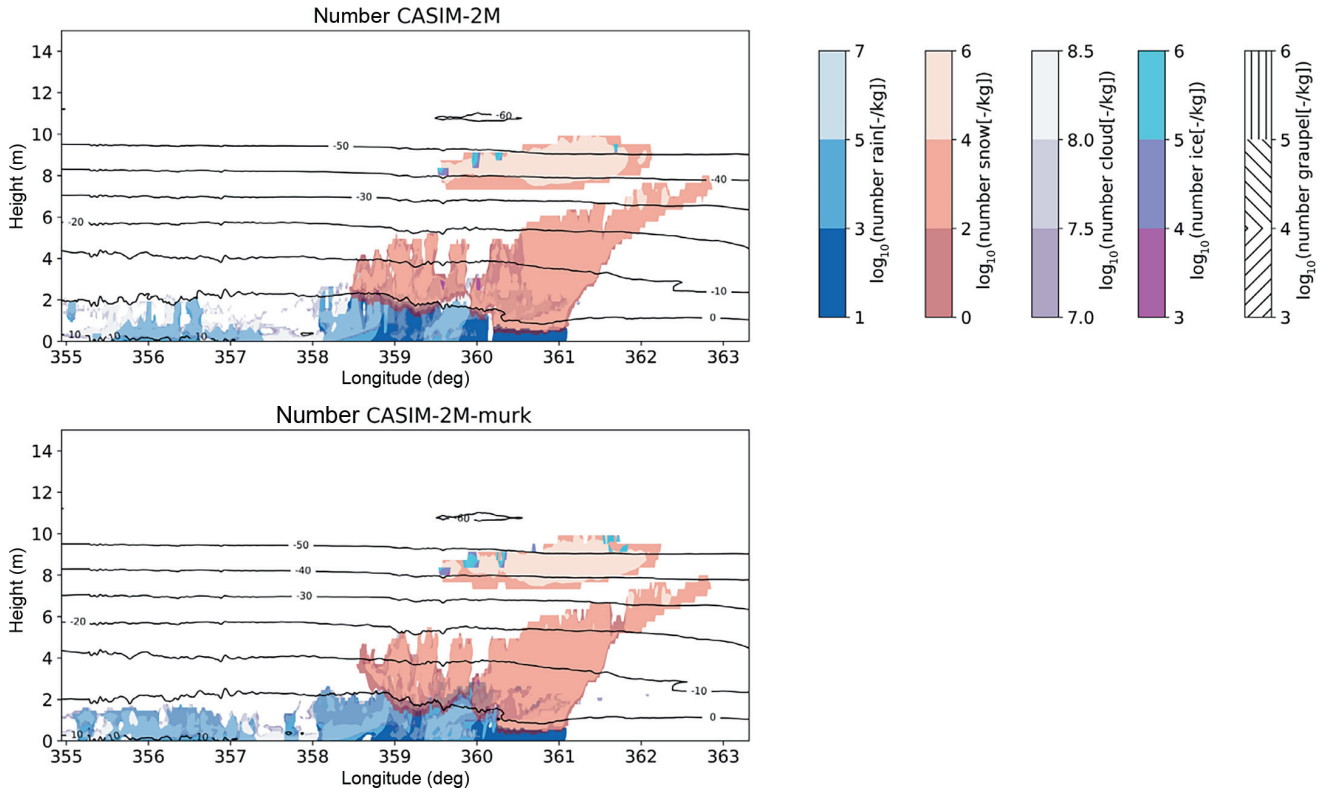

FIGURE 11 Cross-sections for March 27, 2018, 0000 UTC from the United Kingdom Variable grid Cloud AeroSol Interacting Microphysics (CASIM)-2M and CASIM-2M-murk configurations at $T + 12$. Gridbox-mean number mixing ratios are shown

is now present. Changing from prescribed droplet number on activation (CASIM-2M) to one based on MURK aerosol (CASIM-2M-murk) (see Appendix) results in an increase in the amount of supercooled rain in the front (~360°). For the CASIM-2M configurations, cross-sections of number concentration are available (Figure 11). The frontal snow cloud (360–362°) has concentrations of 10^2 to 10^4 kg^{-1} for both CASIM-2M configurations, but CASIM-2M tends to show a greater coverage of lower values than for CASIM-2M-murk. Cloud ice number concentrations of $> 10^4$ kg^{-1} can be seen at the top of the higher detached cirrus cloud (7–10 km) for both, whereas the CASIM-2M, but not CASIM-2M-murk, shows some indication of high cloud ice values in the post-frontal region (e.g., 359.5°, 360°) at a temperature close to −5°C, suggestive that these originate from the Hallett–Mossop (Hallett and Mossop, 1974) secondary ice production process that is included in CASIM. Droplet concentrations are comparable on this plot, given the wide range shown.

4.6 | Darwin tropical storm example

A tropical storm passed through the Darwin domain (1100 UTC March 5, 2017) and shows an example of the model performance at $T + 23$ for each of the configurations. The Global Precipitation Mission precipitation (GPM combined algorithm; Grecu *et al.*, 2016) rate is shown for comparison (Figure 12). Generally, the configurations show peak precipitation rates close to the low-pressure centre arcing south and eastwards into two tails of precipitation. To the north are narrow bands of rain roughly following the isobars. For single-moment CASIM-1M and both the CASIM-2M configurations the low centre is in approximately the same place to the southwest of the Tiwi Islands, whereas for WB it is ~100 km further north. The CASIM-2M configurations (CASIM-2M, CASIM-2M-arcl) display two well-developed precipitation tails with similar levels of precipitation extending towards the low centre, whereas CASIM-1M has a shorter and less distinct northern tail. The WB configuration has two less distinct tails and the precipitation ends 200 km south of the low-pressure centre. As with the UK case, the increased frequency of light rain means that there are larger regions of precipitation rates <1 mm · hr^{-1} in CASIM-2M and CASIM-2M-arcl maps when compared with the the single-moment CASIM-1M and WB configurations. Though in the main precipitation areas to the south of the low-pressure centre frequency of precipitation rates >32 mm · hr^{-1} are present for all configurations, the narrow precipitation arcs in the northern half

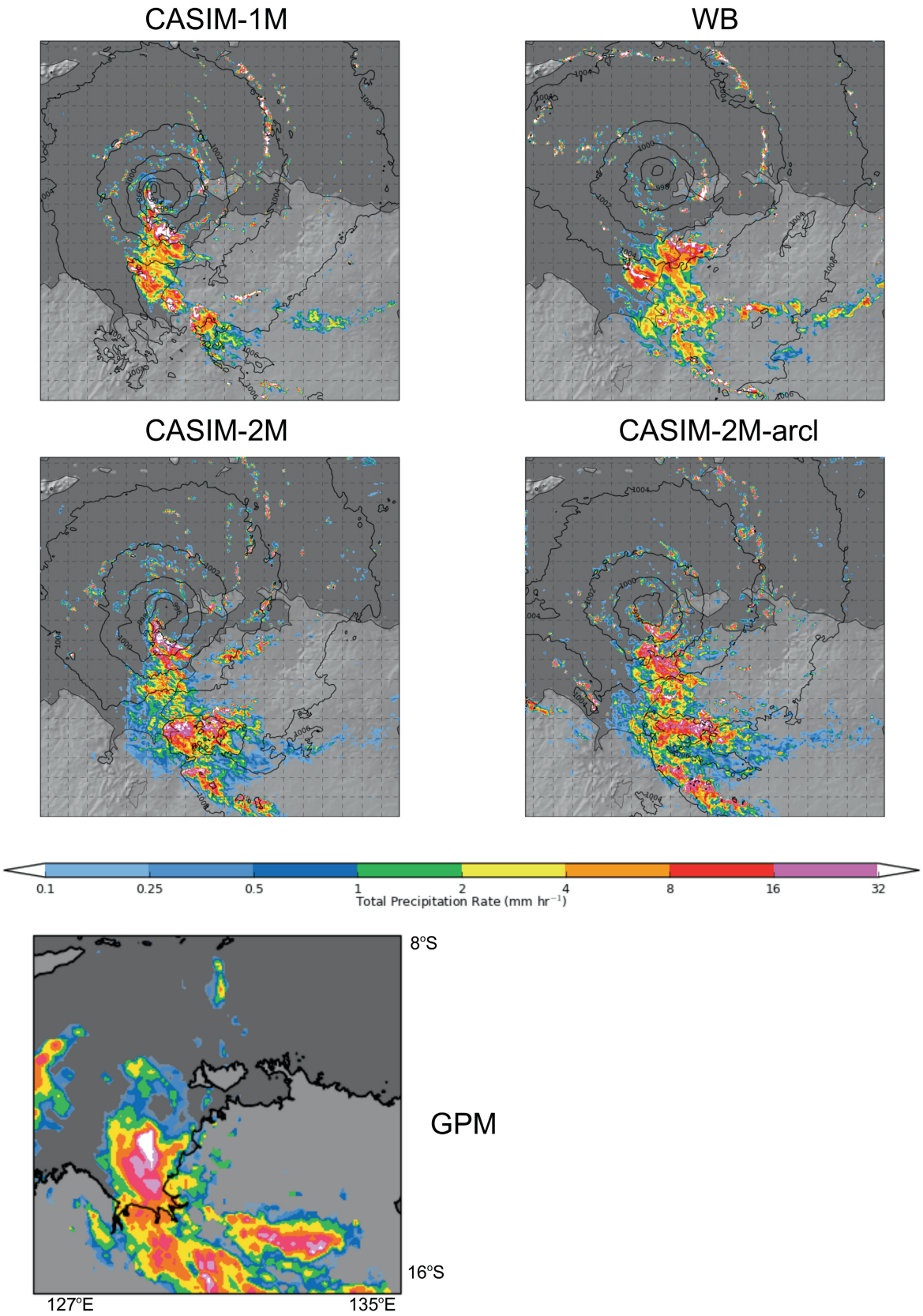

FIGURE 12 Darwin tropical storm example for 1100 UTC March 5, 2017, from the $T + 23$ of Darwin simulation to be coincident with the Global Precipitation Mission (GPM) precipitation measurement. Instantaneous precipitation rates from Cloud AeroSol Interacting Microphysics (CASIM)-1M, Wilson–Ballard (WB), CASIM-2M, and CASIM-2M-arcl are shown. Solid contours are mean sea level pressure (mb).

of the domain show a greater prevalence of >32 mm · hr^{-1} rates that appear to indicate more intense precipitation structures for the single-moment CASIM-1M and WB compared with the CASIM-2M and CASIM-2M-arcl configurations.

An east–west cross-section (1 hr later due to having only 6 hr 3-days' output data available) at 13° S (Figure 13) shows WB has extensive ice cloud above 10 km. CASIM-1M and WB have a narrow range of near-surface rain mass mixing ratios of >0.1 g · kg^{-1}. Introducing double-moment CASIM microphysics breaks up the ice cloud and introduces more variability to the subcloud rain and increases the range of near-surface rain mass mixing ratios. There is also evidence of supercooled rain (127.5° and 129.5° longitude). Using the aerosol climatology to activate cloud droplets (CASIM-2M-arcl) results in less cloud ice and snow than for CASIM-2M and less extensive regions of graupel. An example of a shaft that almost extends down to the surface can be seen at 129.5° longitude. The other obvious difference between the two CASIM-2M configurations is the extensive cloud ice sheet that sits at 17 km in CASIM-2M but is absent in CASIM-2M-arcl. CASIM-2M-arcl produces lower cloud ice number concentrations at cirrus altitudes for similar in-cloud mass because of the lower concentrations of cloud droplets available to freeze homogeneously when using the aerosol climatology, compared with the fixed number configuration (CASIM-2M). This means that the cirrus particles formed by CASIM-2M-arcl are larger then CASIM-2M and will fall faster, leading to reduced cloud ice coverage for CASIM-2M-arcl when compared with CASIM-2M.

Cross-sections of number concentration for the double-moment CASIM configurations (Figure 14) indicate that the cloud ice sheet at 17.5 km in CASIM-2M has number concentrations of 10^6, which will be originating from homogeneous freezing of cloud droplets. Cloud ice is also present around the −5°C level for CASIM-2M-arcl (e.g., 129.5–130°) in both mass and number cross-sections that are indicating the role of the parametrised Hallett–Mossop secondary ice production process. CASIM-2M-arcl tends to exhibit higher number concentrations of rain and cloud water below 2.5 km when compared with CASIM-2M.

The stark difference seen between single and double-moment cloud microphysics has been noted before (Igel *et al.*, 2015), and differences in the areal coverage of lighter precipitation have been linked to differences in rain evaporation (Morrison *et al.*, 2009). Figure 15 shows bin-averaged column integrated rain evaporation rate as a function of integrated rain water column for the instantaneous scene in Figure 12. For the integrated rain water column values exceeding 1 kg · m^{-2} the CASIM-2M configurations indicate evaporation rates up to five times the single-moment (CASIM-1M, WB) configurations for the same integrated rain column. For lower values of the integrated rain column, the single and double-moment evaporation rates are more comparable (within 30% of each other).

5 | DISCUSSION AND CONCLUSIONS

Test-case suites for midlatitude (UK) and tropical (Darwin, Australia) settings using ∼232 simulations of duration 36 hr for domains 1500 × 1500 km^2 have been carried out using the regional configuration of the Met Office UM. The configurations comprised of a control that used the existing operational cloud microphysics (Wilson and Ballard, 1999) and three configurations where the cloud microphysics was changed to the CASIM double-moment scheme using prescribed activated droplet number, aerosol-based droplet number, and a CASIM single-moment set-up. All configurations were built on top of the bimodal cloud fraction scheme.

For the UK, all configurations performed similarly, with cloud cover bias being the only metric that indicated clear improvement for CASIM-2M over WB. For Darwin synoptic near-surface observations of temperature, humidity, wind, and cloud cover, the double-moment CASIM configurations performed as well or better than the control configuration (WB). The CASIM configurations (CASIM-2M, CASIM-2M-murk) exhibited a slight positive precipitation rate bias (0.01–0.02 mm · hr^{-1}) relative to the observations for the UK and −0.5 mm · hr^{-1} for Darwin. Relative to radar-derived rain-rates, the double-moment CASIM configurations provided better agreement with the observations than the WB configuration for the frequency of occurrence of light (<1.5 mm · hr^{-1} and 6 mm · hr^{-1} for the UK and Darwin respectively) and moderate to extreme (>20 mm · hr^{-1}) precipitation rates. In particular, the increased frequency of lighter rain manifests itself as regions of lighter precipitation bridging between islands of more intense precipitation in UK frontal situations. This leads to more coherent frontal precipitation structures.

As a test of the impact of introducing double-moment microphysics, a single-moment configuration of CASIM was also tested in the Darwin suite. The largest differences between the double-moment CASIM and single-moment configurations (WB and CASIM-1M) are seen in the precipitation rate histograms, in which double-moment allows the model to produce more light rain and less intense precipitation relative to the single-moment representations. Even with fixed in-cloud droplet number (CASIM-2M) the cloud water does not contribute much

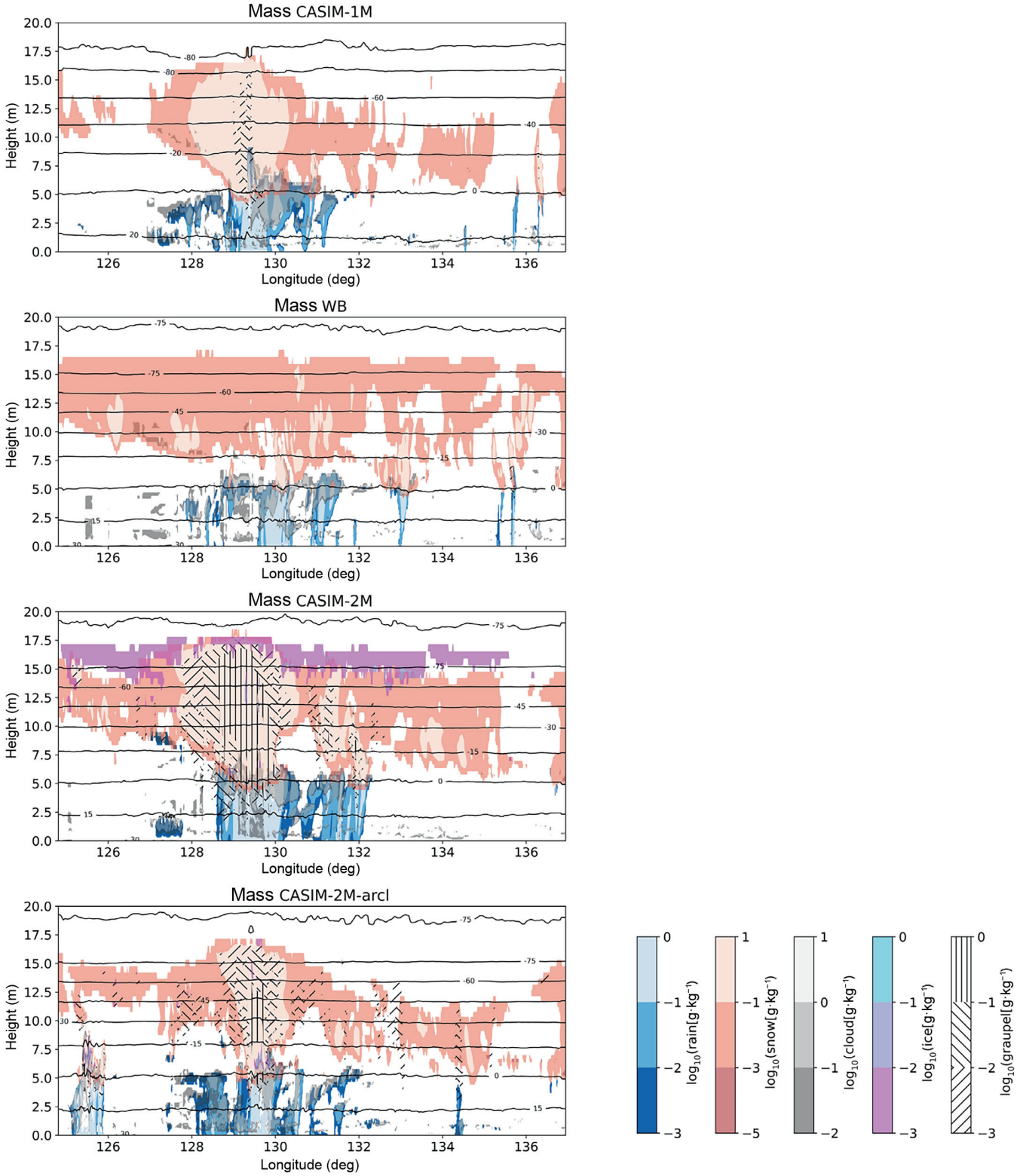

FIGURE 13 Darwin tropical storm example. Cross-section of grid-box-mean mass mixing ratios for Cloud AeroSol Interacting Microphysics (CASIM)-1M, Wilson–Ballard (WB), CASIM-2M, and CASIM-2M-arcll from $T + 24$ output of a Darwin simulation for 1200 UTC March 5, 2017

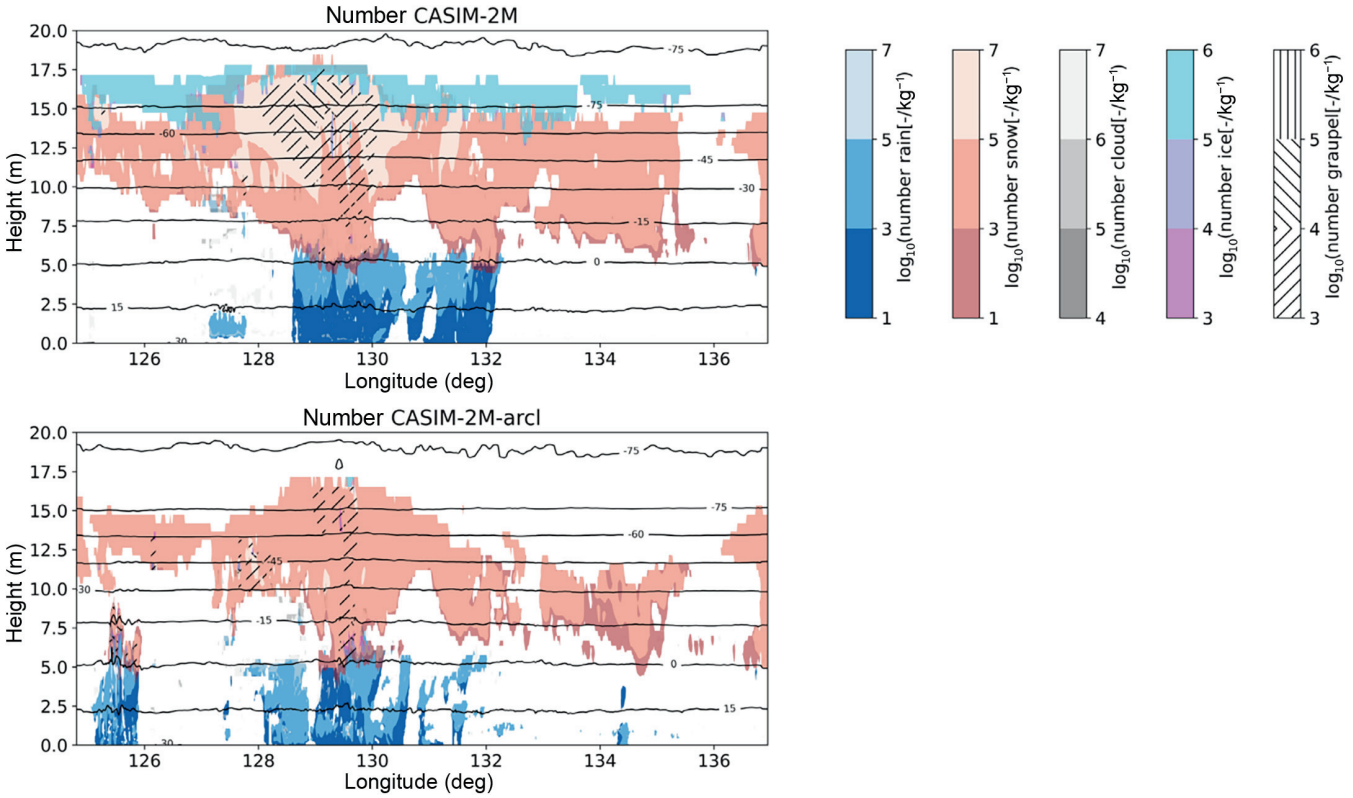

FIGURE 14 Darwin tropical storm example. Cross-section of grid-box-mean number mixing ratios for CASIM-2M and CASIM-2M-arcl from $T + 24$ output of the Darwin simulation for 1200 UTC March 5, 2017

to the precipitation rate; but as the cloud evolves, cloud water gets converted to rain via autoconversion (a function of cloud water amount and number concentration) and accretion (rain mass and cloud mass). These two processes produce a rain number that can vary from $< 1/L$ to $100/L$. Similar arguments hold for cloud ice and snow, which eventually falls through the melting layer to make rain with a number concentration linked to the melting snow number concentration. So, even for configurations where the in-cloud droplet number is fixed, the rain-number concentration can still vary by orders of magnitude for the same rain mass. Consequently, that range in number concentration would lead to different mean sizes with different fall speeds and hence different sedimentation fluxes and evaporation rates below cloud. In the single-moment scheme (WB and CASIM-1M) the same rain mass will always have the same fall speed, sedimentation flux, and evaporation rate for a given subsaturation. Additionally, in the single-moment representations, only mass is sedimented. In the double-moment CASIM configurations the mass and number are sedimented separately using their own weighted fall speeds. This can give an effect of size sorting (because the mass-weighted fall speed is greater than the number-weighted fall speed), where the fewer larger particles get separated from smaller more numerous ones. The increased rain evaporation rate for the larger values of integrated rain water column are indicative of increased evaporation in the tropical convective core regions. This enhanced evaporation for double moment compared with single moment is consistent with previous work (Morrison *et al.*, 2009) and will lead to stronger cold pools that can interact to generate more convection along convergence zones and may partially explain the reduction in extreme precipitation rates exhibited by the single-moment cloud microphysics configurations. In future work we will test the hypothesis that rain evaporation leads to the improved precipitation response by exploring the sensitivity of the precipitation characteristics (intensity distribution and spatial organisation) as a function of rain evaporation. This can be achieved by modifying the droplet size distribution (DSD) shape assumption, rain accreting rain representation, and the ventilation effect, as well as the aerosol environment. The CASIM-1M test also excluded cloud ice that is present for the double-moment configurations. Future tests could include that species to assess the impact of the hydrometeor diversity on the difference in precipitation characteristics between double and single-moment microphysics. Nevertheless, the results presented here clearly demonstrate the benefit of double-moment microphysics in the context of operational

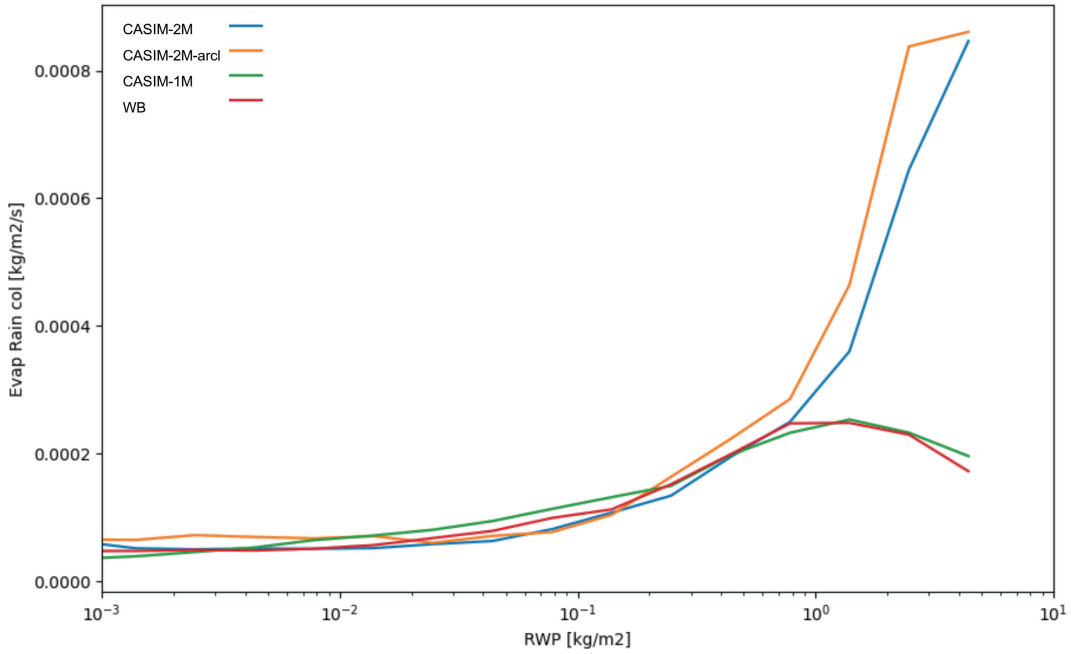

FIGURE 15 Darwin tropical storm example, bin-averaged rain evaporation rate against bins of integrated rain water column for different cloud microphysics configurations – Cloud AeroSol Interacting Microphysics (CASIM)-1M, Wilson–Ballard (WB), CASIM-2M, and CASIM-2M-arcl – using 1200 UTC March 5, 2017, instantaneous data. RWP: rainwater path

NWP and precipitation forecasting, when compared with simpler, more widely operationally used single-moment schemes.

For the short-wave TOA broadband comparisons, CASIM-2M[-arcl, -murk] provided similar agreement with the observations to CASIM-2M (using prescribed in-cloud droplet number). However, for fluxes greater than 700 $W \cdot m^{-2}$, CASIM-2M-murk performs best compared with observations, suggesting that using a more appropriate droplet number through activation of the aerosol could lead to a more realistic cloud albedo. The reduced performance for long-wave radiation with CASIM-2M-arcl, though, suggests that this droplet number concentration sensitivity feeds through to the eventual cirrus characteristics, as exemplified by comparing the cross-sections for CASIM-2M-arcl and CASIM-2M in Figures 13 and 14. This could be through availability of cloud droplets to be frozen homogeneously or by modulating the growth of graupel that can efficiently remove moisture from the atmosphere.

There are a number of discrepancies between the observations and model that can potentially be linked via physical processes and parameter settings in the model. It is not feasible to tackle all of the observational biases in this article, but here some hypotheses will be suggested to explain origin of differences between model and observations.

Model coverage of cirrus is incorrect. The CASIM-2M/-arcl broadband long-wave behaviour of higher (lower) frequency of occurrence at the low flux end of the distribution is consistent with this hypothesis of too much (little) cirrus coverage and/or too high (low) altitude. To test this hypothesis, model runs would need to be conducted that changed the character of the cirrus. There are several ways to achieve this: (i) Modifying the cloud droplet number, which controls the concentration of high-level ice formed through homogeneous freezing; fewer droplets would produce fewer but larger ice crystals that would fall out faster, reducing the ice cloud coverage. (ii) Changing the cloud ice and/or snow sedimentation flux through (a) changing fall speeds, (b) changing the shape parameter of the PSD, (c) changing mass–size relations, (d) modifying the snow aggregation efficiency, and (e) modifying the snow autoconversion rate. (iii) Modifying the process rates related to graupel formation and growth that can dehydrate the upper troposphere by enhancing precipitation efficiency. The changes to these parameters and processes can only be made within the credible observational bounds provided in the literature. The expected result for these tests would directly impact the cirrus coverage and modify the bias in the broadband radiation.

Mass–size relations not appropriate for radar reflectivity weighted particle sizes. The CFADs for the CASIM-2M simulations tend to be too broad. This is interpreted as the mass of particles is too large for a given size. The anomaly is above the melting level and likely related to the snow particles that will dominate the statistics of the CFAD. Reducing the mass of particles as a function of size across

the whole PSD will impact the precipitation rate through changing the mass flux. Recently, coincident in situ radar, independent ice water content, and PSD measurements have been made that indicate that when the best mass–size power-law relationship is derived from radar it has a lower prefactor than when the mass–size relationship is derived from the mass measurement (Heymsfield *et al.*, 2022). This could be replicated in the model by modifying the mass–size power law such that the prefactor decreases with increasing particle size. The predicted change would be that the mass flux of snow remains the same while the CFADs become narrower.

Rain distribution parameters need refinement. The $0.02\ \mathrm{mm \cdot hr^{-1}}$ positive rain bias exhibited by the UKV simulations can be related to the rain DSD shape parameter. If this is modified to produce a narrower DSD then this will reduce the mean fall speed of the rain and enhance any rain evaporation. The outcome of such a test would be to reduce the mean rain bias.

For weather forecasting, the important moments of the hydrometeor PSDs are those required for representing the process rates. For snow with a mass–dimension relation exponent of 2 the important moments will be 1–2.5. Accurate representations of the zeroth and fourth moments are desirable to have but not necessary to have for a useful prediction of precipitation and cloud cover. However, it is becoming increasingly important to accurately predict radar reflectivity as operational data assimilation moves towards routinely ingesting radar data for regional initialisation. Accurate prediction of higher PSD moments depends on improving the parameters controlling the shape of the PSDs and the concentrations of the particles, as well as the mass–size relations and the processes that control the size and number of the distributions, such as aggregation and sedimentation. For the UK and Darwin case suites the snow will dominate above 2 km and 5 km respectively. The CFAD comparisons indicate that for both the UK and Darwin the snow representation is overestimating the radar reflectivity moment (a 33% increase in size can increase dBZ by 5, which would be achieved for a fixed mass by reducing the number concentration by factor of ∼2). Small changes in ice or snow number concentration relative to the uncertainty in these values in terms of measurement (Baumgardner *et al.*, 2017) and from the generation of ice via primary nucleation (Kanji *et al.*, 2017), secondary ice production processes (e.g., Field *et al.*, 2017), or the treatment of aggregation and coagulation of hydrometeors can lead to discrepancies with the higher moments of the distribution. Future challenges lie with constraining and simultaneously improving all (in practice: 0–6) of the moments of the PSD.

For CASIM we have used the prescribed droplet number as well as one derived from an aerosol representation. The case study examples presented in this article show that deriving droplet number through aerosol activation, where aerosol is represented by climatology, does impact the forecasts, particularly in the tropical case studies. Ideally, the forecast will make use of information from the aerosol environment, but doing so requires an accurate aerosol representation, as well as a realistic updraft estimate derived from combining explicitly resolved vertical velocities and a component from subgrid turbulence. The advantage of a prescribed number is that the in-cloud droplet number will be insensitive to grid resolution. For the UM, the regional model configurations are employing grid sizes of 300 to 4500 m in operational or demonstration settings. These resolutions span the grey zone where it is challenging for models to give a grid-resolution-independent estimate of the updraft velocity for use in an activation scheme (e.g., Malavelle *et al.*, 2014). The second aspect is the aerosol representation. For Darwin a monthly mean climatology was used, and so that will not be sensitive to day-to-day weather regime changes. For the UK a prognostic aerosol is available, but it predicts mass only of a blended (sulphate + nitrate + seasalt) aerosol, and so a size needs to be assumed to derive a number concentration. Therefore, in this article the prescribed number on activation is a pragmatic choice, which has been shown to be effective. Including a more detailed aerosol representation is scientifically and computationally challenging for operational NWP but should continue to be an area of active research and development, since there is growing evidence that inclusion of aerosol–cloud interactions is beneficial for NWP (Wilkinson *et al.*, 2013; Jayakumar *et al.*, 2021). The progressive improvement of aerosol available for operational forecasting will mean that CASIM will be able to move to activation based on aerosol (and even ice nucleation based on ice nucleating particle availability) in the future.

As stated in Section 1, as well as prognosing number, other approaches have been suggested, such as a prognostic density for ice to capture the impact of riming (Mansell *et al.*, 2010; Morrison and Milbrandt, 2015) and prognostic shape information for ice based on growth characteristics (Hashino and Tripoli, 2007). Though density errors for graupel are likely of the order of a factor of 2, which impacts size estimates by ∼30%, processes controlling the number concentration are much more uncertain and can lead to errors of potentially orders of magnitude that translate into larger errors in mean size. Initially, we have chosen to not include these additional complexities.

Another issue with multispecies hydrometeor representations is the separation of cloud droplets and ice from rain and snow. This separation means that a process is required to transfer particles from the smaller to

the larger species, when in reality there is a continuum. For droplets, the distinction is due to the larger rapid response of cloud droplets to humidity changes, relative to ice, and the influence of aerosol activation. For ice, the slower response to humidity changes relative to liquid means that both cloud ice and snow could be considered together for diffusional growth; however, the snow species represents aggregates that grow in size predominantly by self-aggregation whereas the cloud ice species represents single pristine crystals that grow in size mainly by diffusional growth. The geometric distinction between pristine monomer cloud ice and aggregated snow is a more natural separation that can be represented by autoconversion from ice to snow. Once aggregates are formed they forget about their monomer characteristics and tend towards similar power-law values to describe their geometry and dominate ice-phase species for clouds that are a few kilometres in thickness (Korolev and Isaac, 2003; Westbrook *et al.*, 2004).

In this article we concentrated on the double-moment configuration of CASIM without aerosol tracers. By focusing operational developments on the double-moment configuration we were able to optimise the integration time for this version of CASIM, which includes an additional eight prognostics tracers (six hydrometeor moments and two cloud fractions), so that the integration time for the CASIM configuration forecasts is 1.3 times that of the operational single-moment configuration based on WB. Future optimisations could take advantage of GPU-based approaches that are being explored (Zhang *et al.*, 2021).

Previous operational single-moment cloud microphysics configurations of the Met Office Regional Model (Bush et al 2020) employed separate configurations of the regional model for the Tropics and midlatitudes. By including CASIM double-moment cloud microphysics with the bimodal cloud fraction scheme, similar or improved performance has been demonstrated in both the Tropics and midlatitudes using the same configuration relative to single-moment cloud microphysics. The CASIM configuration introduced here is the configuration proposed to be adopted for operational use in 2023, and the full documentation of the performance of this configuration against the current operational configuration across spatial and temporal time-scales in different regimes is documented in Bush et al. (2020).

Finally, the proposed introduction of the CASIM double-moment microphysics into the operational setting crosses a hurdle that makes it easier to incrementally introduce increasingly complex links to aerosol such as prognostic double-moment cloud condensation nuclei and ice nucleating particles if these are found to improve the forecast skill.

AUTHOR CONTRIBUTIONS

Paul R. Field: conceptualization; formal analysis; software; validation; visualization; writing – original draft; writing – review and editing. **Adrian Hill:** conceptualization; methodology; software; validation; writing – original draft; writing – review and editing. **Ben Shipway:** conceptualization; methodology; software; writing – original draft. **Kalli Furtado:** software; validation; writing – original draft; writing – review and editing. **Jonathan Wilkinson:** software; validation; writing – original draft. **Annette Miltenberger:** software; validation; writing – original draft; writing – review and editing. **Hamish Gordon:** software; validation; writing – original draft; writing – review and editing. **Daniel P. Grosvenor:** software; validation; writing – original draft; writing – review and editing. **Robin Stevens:** software; validation; writing – original draft; writing – review and editing. **Kwinten Van Weverberg:** software; validation; writing – original draft.

ACKNOWLEDGEMENTS

The development of CASIM has been a considerable effort by many people over several years: Ben Shipway wrote the original CASIM code for MONC; Adrian Hill contributed to the original code, UM code development, refactoring, and improving optimisation; Paul Field contributed to coupling to UM cloud schemes and science changes to CASIM code and bespoke validation; Jonathan Wilkinson and Kalli Furtado, in Atmospheric Processes and Parametrizations, contributed to code development; and Annette Miltenberger, Dan Grosvenor, Robin Stevens, and Hamish Gordon contributed to code development and validation. We would also like to thank the RMED team for providing case study and verification suites, Michele Guidolin for openMP and optimisation work, the UM systems team for ongoing trunk support, and Charmaine Franklin (Bureau of Meteorology) for providing the CPOL dataset.

Robin Stevens gratefully acknowledges support from the European Union's Seventh Framework Programme (FP7/2007-2013) with the project "Impact of Biogenic versus Anthropogenic Emissions on Clouds and Climate: Towards a Holistic Understanding" (BACCHUS; grant no. 603445). Hamish Gordon acknowledges support from the NASA Roses program under grant nos. 80NSSC19K0949 and 80NSSC21K1344 and from the NERC CLARIFY project (NE/L013584/1). Paul R. Field would like to acknowledge the PRIMAVERA project, funded by the European Union's Horizon 2020 program, grant agreement no. 641727, and the UK–China Research and Innovation Partnership Fund through the Met Office

Climate Science for Service Partnership (CSSP) China as part of the Newton Fund.

Owing to intellectual property rights restrictions, we cannot provide the source code or documentation papers for the UM. The Met Office UM is available for use under licence. A number of research organisations and national meteorological services use the UM in collaboration with the Met Office to undertake basic atmospheric process research, produce forecasts, and develop the UM code. To apply for a licence, see http://www.metoffice.gov.uk/research/modelling-systems/unified-model. CASIM is open source (BSD3 licence) and it is available from code.metoffice.gov.uk, which requires registration.

Vn12.0 of the UM was used with the following branches:

```
casim_sources = fcm:casim.xm/branches/dev/paulfield/
                r8687_vn0.4_casim_pkg@9660
um_sources = fcm:um.xm/branches/pkg/paulfield/
             vn12.0_casim_ra3@109288
           = fcm:um.xm/branches/dev/adrianlock/
             vn12.0_grid_indep_fa_blend@102514
```

These have since been committed to the trunk for both the UM@vn13.0 and casim@vn1.0 releases.

The model suites, including configuration settings and case dates, are available for UKV at https://code.metoffice.gov.uk/trac/roses-u/browser/c/n/8/0/0/trunk?rev=227564 and Darwin at https://code.metoffice.gov.uk/trac/roses-u/browser/c/n/8/5/1/trunk?rev=225943. These suites use vn12.0 of the UM.

Model output from the suites used is available on MASS tape archive and can be accessed upon request by obtaining a login on UK's environmental science data analysis facility at jasmin.ac.uk.

ORCID

Paul R. Field https://orcid.org/0000-0001-8528-0088
Adrian Hill https://orcid.org/0000-0002-7444-9367
Jonathan Wilkinson https://orcid.org/0000-0002-6906-4999
Annette Miltenberger https://orcid.org/0000-0003-3320-4272
Hamish Gordon https://orcid.org/0000-0002-1822-3224
Robin Stevens https://orcid.org/0000-0002-8737-6988
Kwinten Van Weverberg https://orcid.org/0000-0002-5397-7320

REFERENCES

Abel, S.J. and Shipway, B.J. (2007) A comparison of cloud-resolving model simulations of trade wind cumulus with aircraft observations taken during RICO. *Quarterly Journal of the Royal Meteorological Society*, 133, 781-794.

Abdul-Razzak, H. and Ghan, S. (2000) A parameterization of aerosol activation 2. Multiple aerosol types. *Journal of Geophysical Research-Atmospheres*, 105(D5), 6837–6844. https://doi.org/10.1029/1999JD901161.

Atkinson, J.D., Murray, B.J., Woodhouse, M.T., Whale, T.F., Baustian, K.J., Carslaw, K.S., Dobbie, S., O'Sullivan, D. and Malkin, T.L. (2013) The importance of feldspar for ice nucleation by mineral dust in mixed-phase clouds. *Nature*, 498(7454), 355–358. https://doi.org/10.1038/nature12278.

Baumgardner, D., Avallone, L., Bansemer, A., Borrmann, S., Brown, P., Bundke, U., Chuang, P.Y., Cziczo, D., Field, P., Gallagher, M., Gayet, J.-F., Heymsfield, A., Korolev, A., Krämer, M., McFarquhar, G., Mertes, S., Möhler, O., Lance, S., Lawson, P., Petters, M.D., Pratt, K., Roberts, G., Rogers, D., Stetzer, O., Stith, J., Strapp, W., Twohy, C. and Wendisch, M. (2017) In situ, airborne instrumentation addressing and solving measurement problems in ice clouds. *Bulletin of the American Meteorological Society*, 93(2), E529–E534. https://doi.org/10.1175/BAMS-D-11-00123.1.

Beheng, K.D. (1994) A parameterization of warm cloud microphysical conversion processes. *Atmospheric Research*, 33(1-4), 193–206. https://doi.org/10.1016/0169-8095(94)90020-5.

Bellouin, N., Mann, G.W., Woodhouse, M.T., Johnson, C., Carslaw, K.S. and Dalvi, M. (2013) Impact of the modal aerosol scheme GLOMAP-mode on aerosol forcing in the hadley centre global environmental model. *Atmospheric Chemistry and Physics*, 13(6), 3027–3044. https://doi.org/10.5194/acp-13-3027-2013.

Bellouin, N., Rae, J., Jones, A., Johnson, C., Haywood, J. and Boucher, O. (2011) Aerosol forcing in the climate model intercomparison project (cmip5) simulations by hadgem2-es and the role of ammonium nitrate. *Journal of Geophysical Research-Atmospheres*, 116, D20206. https://doi.org/10.1029/2011JD016074.

Best, M.J., Pryor, M., Clark, D.B., Rooney, G., Essery, R.L.H., Menard, C.B., Edwards, J.M., Hendry, M., Porson, A. and Gedney, N. (2011) The joint uk land environment simulator (jules), model description - part 1: energy and water fluxes. *Geoscientific Model Development*, 4(3), 677–699. https://doi.org/10.5194/gmd-4-677-2011.

Bigg, E.K. (1953) The supercooling of water. *Proceedings of the Physical Society. Section B*, 66(8), 688–694. https://doi.org/10.1088/0370-1301/66/8/309.

Boutle, I.A., Eyre, J.E.J. and Lock, A.P. (2014) Seamless stratocumulus simulation across the turbulent gray zone. *Monthly Weather Review*, 142(4), 1655–1668. https://doi.org/10.1175/MWR-D-13-00229.1.

Bush, M., Allen, T., Bain, C., Boutle, I., Edwards, J., Finnenkoetter, A., Franklin, C., Hanley, K., Lean, H., Lock, A., Manners, J., Mittermaier, M., Morcrette, C., North, R., Petch, J., Short, C., Vosper, S., Walters, D., Webster, S., Weeks, M., Wilkinson, J., Wood, N. and Zerroukat, M. (2020) The first met office unified model-JULES regional atmosphere and land configuration, RAL1. *Geoscientific Model Development*, 13(4), 1999–2029. https://doi.org/10.5194/gmd-13-1999-2020.

Cohard, J. and Pinty, J. (2000) A comprehensive two-moment warm microphysical bulk scheme. I: Description and tests. *Quarterly Journal of the Royal Meteorological Society*, 126(566), 1815–1842. https://doi.org/10.1256/smsqj.56613.

Cooper, W.A. (1987) Ice initiation in natural clouds. In: *Precipitation enhancement—A scientific challenge*. Meteorological Monographs, Vol. 43. New York: Springer, pp. 29–32.

Cotton, R.J., Field, P.R., Ulanowski, Z., Kaye, P.H., Hirst, E., Greenaway, R.S., Crawford, I., Crosier, J. and Dorsey, J. (2013) The effective density of small ice particles obtained from in situ aircraft observations of mid-latitude cirrus. *Quarterly Journal of the Royal Meteorological Society*, 139, 1923-1934. https://doi.org/10.1002/qj.2058

Cullen, M., Davies, T., Mawson, M., James, J., Coulter, S. and Malcolm, A. (1997) An overview of numerical methods for the next generation UK NWP and climate model. In: Lin, C.A., Laprise, R. and Ritchie, H. (Eds.) *Numerical methods in atmospheric and ocean modelling: the Andre J. Robert memorial volume*. Ottawa: Canadian Meteorological and Oceanographic Society, pp. 425–444.

Davies, T., Cullen, M., Malcolm, A., Mawson, M., Staniforth, A., White, A. and Wood, N. (2005) A new dynamical core for the met office's global and regional modelling of the atmosphere. *Quarterly Journal of the Royal Meteorological Society*, 131(608), 1759–1782. https://doi.org/10.1256/qj.04.101.

Dearden, C., Hill, A., Coe, H. and Choularton, T. (2018) The role of droplet sedimentation in the evolution of low-level clouds over southern west africa. *Atmospheric Chemistry and Physics*, 18(19), 14253–14269. https://doi.org/10.5194/acp-18-14253-2018.

DeMott, P.J., Prenni, A.J., Liu, X., Kreidenweis, S.M., Petters, M.D., Twohy, C.H., Richardson, M.S., Eidhammer, T. and Rogers, D.C. (2010) Predicting global atmospheric ice nuclei distributions and their impacts on climate. *Proceedings of the National Academy of Sciences of the United States of America*, 107(25), 11217–11222. https://doi.org/10.1073/pnas.0910818107.

DeMott, P.J., Prenni, A.J., McMeeking, G.R., Sullivan, R.C., Petters, M.D., Tobo, Y., Niemand, M., Möhler, O., Snider, J.R., Wang, Z. and Kreidenweis, S.M. (2015) Integrating laboratory and field data to quantify the immersion freezing ice nucleation activity of mineral dust particles. *Atmospheric Chemistry and Physics*, 15(1), 393–409. https://doi.org/10.5194/acp-15-393-2015.

Doelling, D.R., Loeb, N.G., Keyes, D.F., Nordeen, M.L., Morstad, D., Nguyen, C., Wielicki, B.A., Young, D.F. and Sun, M. (2013) Geostationary enhanced temporal interpolation for CERES flux products. *Journal of Atmospheric and Oceanic Technology*, 30(6), 1072–1090. https://doi.org/10.1175/JTECH-D-12-00136.1.

Dowell, D.C., Alexander, C.R., James, E.P., Weygandt, S.S., Benjamin, S.G., Manikin, G.S., Blake, B.T., Brown, J.M., Olson, J.B., Hu, M., Smirnova, T.G., Ladwig, T., Kenyon, J.S., Ahmadov, R., Turner, D.D., Duda, J.D. and Alcott, T.I. (2022) The high-resolution rapid refresh (HRRR): an hourly updating convection-allowing forecast model. Part I: motivation and system description. *Weather and Forecasting*, 37(8), 1371–1395. https://doi.org/10.1175/WAF-D-21-0151.1.

Ferrier, B. (1994) A double-moment multiple-phase 4-class bulk ice scheme.1. Description. *Journal of the Atmospheric Sciences*, 51(2), 249–280.

Field, P.R. and Heymsfield, A.J. (2015) Importance of snow to global precipitation. *Geophysical Research Letters*, 42(21), 9512–9520. https://doi.org/10.1002/2015GL065497.

Field, P.R., Hill, A.A., Furtado, K. and Korolev, A. (2014) Mixed-phase clouds in a turbulent environment. Part 2: analytic treatment. *Quarterly Journal of the Royal Meteorological Society*, 140(680), 870–880. https://doi.org/10.1002/qj.2175.

Field, P.R., Lawson, R.P., Brown, P.R.A., Lloyd, G., Westbrook, C., Moisseev, D., Miltenberger, A., Nenes, A., Blyth, A., Choularton, T., Connolly, P., Buehl, J., Crosier, J., Cui, Z., Dearden, C., DeMott, P., Flossmann, A., Heymsfield, A., Huang, Y., Kalesse, H., Kanji, Z.A., Korolev, A., Kirchgaessner, A., Lasher-Trapp, S., Leisner, T., McFarquhar, G., Phillips, V., Stith, J. and Sullivan, S. (2017) Secondary ice production: current state of the science and recommendations for the future. In: Baumgardner, D., McFarquhar, G. and Heymsfield, A. (Eds.) *Ice formation and evolution in clouds and precipitation: measurement and modeling challenges*. Meteorological Monographs, Vol. 58. New York: Springer. https://doi.org/10.1175/AMSMONOGRAPHS-D-16-0014.1.

Furtado, K., Field, P.R., Boutle, I.A., Morcrette, C.J. and Wilkinson, J.M. (2016) A physically based subgrid parameterization for the production and maintenance of mixed-phase clouds in a general circulation model. *Journal of the Atmospheric Sciences*, 73(1), 279–291. https://doi.org/10.1175/JAS-D-15-0021.1.

Ghan, S.J. and Easter, R.C. (2006) Impact of cloud-borne aerosol representation on aerosol direct and indirect effects. *Atmospheric Chemistry and Physics*, 6, 4163–4174. https://doi.org/10.5194/acp-6-4163-2006.

Gordon, H., Field, P.R., Abel, S.J., Barrett, P., Bower, K., Crawford, I., Cui, Z., Grosvenor, D.P., Hill, A.A., Taylor, J., Wilkinson, J., Wu, H. and Carslaw, K.S. (2020) Development of aerosol activation in the double-moment unified model and evaluation with clarify measurements. *Atmospheric Chemistry and Physics*, 20(18), 10997–11024. https://doi.org/10.5194/acp-20-10997-2020.

Gordon, H., Field, P.R., Abel, S.J., Dalvi, M., Grosvenor, D.P., Hill, A.A., Johnson, B.T., Miltenberger, A.K., Yoshioka, M. and Carslaw, K.S. (2018) Large simulated radiative effects of smoke in the south-east Atlantic. *Atmospheric Chemistry and Physics*, 18(20), 15261–15289. https://doi.org/10.5194/acp-18-15261-2018.

Gray, M.E.B., Petch, J., Derbyshire, S.H., Brown, A.R., Lock, A.P., Swann, H.A. and Brown, P.R.A. (2001) *Version 2.3 of the met office large eddy model. Part II. Scientific documentation. Technical note*, Vol. 276. Exeter: United Kingdom Met Office.

Hallett, J. and Mossop, S. (1974) Production of secondary ice particles during riming. *Journal of Applied Meteorology*, 19, 950–966.

Harrison, D.L., Driscoll, S.J. and Kitchen, M. (2000) Improving precipitation estimates from weather radar using quality control and correction techniques. *Meteorological Applications*, 7(2), 135–144. https://doi.org/10.1017/S1350482700001468.

Hashino, T. and Tripoli, G.J. (2007) The spectral ice habit prediction system (SHIPS). Part 1: model description and simulation of the vapor deposition process. *Journal of the Atmospheric Sciences*, 64(7), 2210–2237. https://doi.org/10.1175/JAS3963.1.

Hawker, R.E., Miltenberger, A.K., Johnson, J.S., Wilkinson, J.M., Hill, A.A., Shipway, B.J., Field, P.R., Murray, B.J. and Carslaw, K.S. (2021) Model emulation to understand the joint effects of ice-nucleating particles and secondary ice production on deep convective anvil cirrus. *Atmospheric Chemistry and Physics*, 21(23), 17315–17343. https://doi.org/10.5194/acp-21-17315-2021.

Hersbach, H., Bell, B., Berrisford, P., Hirahara, S., Horányi, A., Muñoz-Sabater, J., Nicolas, J., Peubey, C., Radu, R., Schepers, D., Simmons, A., Soci, C., Abdalla, S., Abellan, X., Balsamo, G., Bechtold, P., Biavati, G., Bidlot, J., Bonavita, M., De Chiara, G., Dahlgren, P., Dee, D., Diamantakis, M., Dragani, R., Flemming, J., Forbes, R., Fuentes, M., Geer, A., Haimberger, L., Healy, S.,

Hogan, R.J., Hólm, E., Janisková, M., Keeley, S., Laloyaux, P., Lopez, P., Lupu, C., Radnoti, G., de Rosnay, P., Rozum, I., Vamborg, F., Villaume, S. and Thépaut, J.-N. (2020) The era5 global reanalysis. *Quarterly Journal of the Royal Meteorological Society*, 146(730), 1999–2049. https://doi.org/10.1002/qj.3803.

Heymsfield, A., Bansemer, A., Heymsfield, G., Noone, D., Grecu, M. and Toohey, D. (2022) Relationship of multiwavelength radar measurements to ice microphysics from the IMPACTS field program. *Journal of Applied Meteorology and Climatology*. https://doi.org/10.1175/JAMC-D-22-0057.1

Hill, A.A., Shipway, B.J. and Boutle, I.A. (2015) How sensitive are aerosol-precipitation interactions to the warm rain representation? *Journal of Advances in Modeling Earth Systems*, 7(3), 987–1004. https://doi.org/10.1002/2014MS000422.

Igel, A.L., Igel, M.R. and van den Heever, S.C. (2015) Make it a double? sobering results from simulations using single-moment microphysics schemes. *Journal of the Atmospheric Sciences*, 72(2), 910–925. https://doi.org/10.1175/JAS-D-14-0107.1.

Jayakumar, A., Gordon, H., Francis, T., Hill, A.A., Mohandas, S., Sandeepan, B.S., Mitra, A.K. and Beig, G. (2021) Delhi model with chemistry and aerosol framework (dm-chem) for high-resolution fog forecasting. *Quarterly Journal of the Royal Meteorological Society*, 147(741), 3957–3978. https://doi.org/10.1002/qj.4163.

Jones, A., Roberts, D. and Slingo, A. (1994) A climate model study of indirect radiative forcing by anthropogenic sulfate aerosols. *Nature*, 370(6489), 450–453. https://doi.org/10.1038/370450a0.

Jouan, C., Milbrandt, J.A., Vaillancourt, P.A., Chosson, F. and Morrison, H. (2020) Adaptation of the predicted particles properties (p3) microphysics scheme for large-scale numerical weather prediction. *Weather and Forecasting*, 35(6), 2541–2565. https://doi.org/10.1175/WAF-D-20-0111.1.

Kanji, Z.A., Ladino, L.A., Wex, H., Boose, Y., Burkert-Kohn, M., Cziczo, D.J. and Kraemer, M. (2017) Overview of ice nucleating particles. In: Baumgardner, D., McFarquhar, G. and Heymsfield, A. (Eds.) *Ice formation and evolution in clouds and precipitation: measurement and modeling challenges*. Meteorological Monographs, Vol. 58. New York: Springer. https://doi.org/10.1175/AMSMONOGRAPHS-D-16-0006.1.

Khairoutdinov, M. and Kogan, Y. (2000) A new cloud physics parameterization in a large-eddy simulation model of marine stratocumulus. *Monthly Weather Review*, 128(1), 229–243. https://doi.org/10.1175/1520-0493(2000)128<0229:ANCPPI>2.0.CO;2.

Kogan, Y. (2013) A cumulus cloud microphysics parameterization for cloud-resolving models. *Journal of the Atmospheric Sciences*, 70(5), 1423–1436. https://doi.org/10.1175/JAS-D-12-0183.1.

Korolev, A. and Isaac, G. (2003) Roundness and aspect ratio of particles in ice clouds. *Journal of the Atmospheric Sciences*, 60(15), 1795–1808. https://doi.org/10.1175/1520-0469(2003)060<1795:RAAROP>2.0.CO;2.

Lean, H.W., Clark, P.A., Dixon, M., Roberts, N.M., Fitch, A., Forbes, R. and Halliwell, C. (2008) Characteristics of high-resolution versions of the met office unified model for forecasting convection over the united kingdom. *Monthly Weather Review*, 136(9), 3408–3424. https://doi.org/10.1175/2008MWR2332.1.

Lock, A., Brown, A., Bush, M., Martin, G. and Smith, R. (2000) A new boundary layer mixing scheme. Part I: scheme description and single-column model tests. *Monthly Weather Review*, 128(9), 3187–3199. https://doi.org/10.1175/1520-0493(2000)128<3187:ANBLMS>2.0.CO;2.

Lohmann, U., Stier, P., Hoose, C., Ferrachat, S., Kloster, S., Roeckner, E. and Zhang, J. (2007) Cloud microphysics and aerosol indirect effects in the global climate model ECHAM5-HAM. *Atmospheric Chemistry and Physics*, 7(13), 3425–3446. https://doi.org/10.5194/acp-7-3425-2007.

Louf, V., Protat, A., Warren, R.A., Collis, S.M., Wolff, D.B., Raunyiar, S., Jakob, C. and Petersen, W.A. (2019) An integrated approach to weather radar calibration and monitoring using ground clutter and satellite comparisons. *Journal of Atmospheric and Oceanic Technology*, 36(1), 17–39. https://doi.org/10.1175/JTECH-D-18-0007.1.

Malavelle, F.F., Haywood, J.M., Field, P.R., Hill, A.A., Abel, S.J., Lock, A.P., Shipway, B.J. and McBeath, K. (2014) A method to represent subgrid-scale updraft velocity in kilometer-scale models: Implication for aerosol activation. *Journal of Geophysical Research-Atmospheres*, 119(7), 4149–4173. https://doi.org/10.1002/2013JD021218.

Mann, G.W., Carslaw, K.S., Spracklen, D.V., Ridley, D.A., Manktelow, P.T., Chipperfield, M.P., Pickering, S.J. and Johnson, C.E. (2010) Description and evaluation of glomap-mode: a modal global aerosol microphysics model for the ukca composition-climate model. *Geoscientific Model Development*, 3(2), 519–551. https://doi.org/10.5194/gmd-3-519-2010.

Manners, J., Edwards, J.M., Hill, P. and Thelen, J.-C. (2018) *SOCRATES (suite of community radiative transfer codes based on edwards and slingo) technical guide*. UK, Available at: Met Office. https://code.metoffice.gov.uk/trac/socrates.

Mansell, E.R., Ziegler, C.L. and Bruning, E.C. (2010) Simulated electrification of a small thunderstorm with two-moment bulk microphysics. *Journal of the Atmospheric Sciences*, 67(1), 171–194. https://doi.org/10.1175/2009JAS2965.1.

Martin, G., Johnson, D. and Spice, A. (1994) The measurement and parameterization of effective radius of droplets in warm stratocumulus clouds. *Journal of the Atmospheric Sciences*, 51(13), 1823–1842. https://doi.org/10.1175/1520-0469(1994)051<1823:TMAPOE>2.0.CO;2.

McCaul, E.W., Jr., Goodman, S.J., LaCasse, K.M. and Cecil, D.J. (2009) Forecasting lightning threat using cloud-resolving model simulations. *Weather and Forecasting*, 24(3), 709–729. https://doi.org/10.1175/2008WAF2222152.1.

Meyers, M., Walko, R., Harrington, J. and Cotton, W. (1997) New RAMS cloud microphysics parameterization.2. The two-moment scheme. *Atmospheric Research*, 45(1), 3–39. https://doi.org/10.1016/S0169-8095(97)00018-5.

Milbrandt, J. and Yau, M. (2005a) A multimoment bulk microphysics parameterization. Part I: Analysis of the role of the spectral shape parameter. *Journal of the Atmospheric Sciences*, 62(9), 3051–3064. https://doi.org/10.1175/JAS3534.1.

Milbrandt, J. and Yau, M. (2005b) A multimoment bulk microphysics parameterization. Part II: A proposed three-moment closure and scheme description. *Journal of the Atmospheric Sciences*, 62(9), 3065–3081. https://doi.org/10.1175/JAS3535.1.

Miltenberger, A.K., Field, P.R., Hill, A.A., Rosenberg, P., Shipway, B.J., Wilkinson, J.M., Scovell, R. and Blyth, A.M. (2018) Aerosol-cloud interactions in mixed-phase convective clouds - part 1: aerosol perturbations. *Atmospheric Chemistry and Physics*, 18(5), 3119–3145. https://doi.org/10.5194/acp-18-3119-2018.

Miltenberger, A.K., Field, P.R., Hill, A.H. and Heymsfield, A.J. (2020) Vertical redistribution of moisture and aerosol in orographic

mixed-phase clouds. *Atmospheric Chemistry and Physics*, 20(13), 7979–8001. https://doi.org/10.5194/acp-20-7979-2020.

Morrison, H. and Gettelman, A. (2008) A new two-moment bulk stratiform cloud microphysics scheme in the community atmosphere model, version 3 (CAM3). Part I: description and numerical tests. *Journal of Climate*, 21(15), 3642–3659. https://doi.org/10.1175/2008JCLI2105.1.

Morrison, H. and Milbrandt, J.A. (2015) Parameterization of cloud microphysics based on the prediction of bulk ice particle properties. Part I: scheme description and idealized tests. *Journal of the Atmospheric Sciences*, 72(1), 287–311. https://doi.org/10.1175/JAS-D-14-0065.1.

Morrison, H., Thompson, G. and Tatarskii, V. (2009) Impact of cloud microphysics on the development of trailing stratiform precipitation in a simulated squall line: comparison of one- and two-moment schemes. *Monthly Weather Review*, 137(3), 991–1007. https://doi.org/10.1175/2008MWR2556.1.

Musil, D. (1970) Computer modelling of hailstone growth in feeder clouds. *Journal of Atmospheric Science*, 27, 474–482.

Niemand, M., Möhler, O., Vogel, B., Vogel, H., Hoose, C., Connolly, P., Klein, H., Bingemer, H., DeMott, P., Skrotzki, J. and Leisner, T. (2012) A particle-surface-area-based parameterization of immersion freezing on desert dust particles. *Journal of the Atmospheric Sciences*, 69(10), 3077–3092. https://doi.org/10.1175/JAS-D-11-0249.1.

Poku, C., Ross, A.N., Hill, A.A., Blyth, A.M. and Shipway, B. (2021) Is a more physical representation of aerosol activation needed for simulations of fog? *Atmospheric Chemistry and Physics*, 21(9), 7271–7292. https://doi.org/10.5194/acp-21-7271-2021.

Reisner, J., Rasmussen, R. and Bruintjes, R. (1998) Explicit forecasting of supercooled liquid water in winter storms using the MM5 mesoscale model. *Quarterly Journal of the Royal Meteorological Society*, 124(548), 1071–1107. https://doi.org/10.1256/smsqj.54803.

Rotstayn, L. (1997) A physically based scheme for the treatment of stratiform clouds and precipitation in large-scale models.1. Description and evaluation of the microphysical processes. *Quarterly Journal of the Royal Meteorological Society*, 123(541), 1227–1282. https://doi.org/10.1002/qj.49712354106.

Scovell, R. and Al-Sakka, H. (2016) A point cloud method for retrieval of high-resolution 3D gridded reflectivity from weather radar networks for air traffic management. *Journal of Atmospheric and Oceanic Technology*, 33(3), 461–479. https://doi.org/10.1175/JTECH-D-15-0051.1.

Seifert, A. and Beheng, K. (2006) A two-moment cloud microphysics parameterization for mixed-phase clouds. Part 1: model description. *Meteorology and Atmospheric Physics*, 92(1-2), 45–66. https://doi.org/10.1007/s00703-005-0112-4.

Senior, C. and Mitchell, J. (1993) Carbon-dioxide and climate - the impact of cloud parameterization. *Journal of Climate*, 6(3), 393–418. https://doi.org/10.1175/1520-0442(1993)006<0393:CDACTI>2.0.CO;2.

Shipway, B.J. and Hill, A.A. (2012) Diagnosis of systematic differences between multiple parametrizations of warm rain microphysics using a kinematic framework. *Quarterly Journal of the Royal Meteorological Society*, 138(669), 2196–2211. https://doi.org/10.1002/qj.1913.

Smith, R. (1990) A scheme for predicting layer clouds and their water-content in a general-circulation model. *Quarterly Journal of the Royal Meteorological Society*, 116(492), 435–460. https://doi.org/10.1256/smsqj.49209.

Stein, T.H.M., Scovell, R.W., Hanley, K.E., Lean, H.W. and Marsden, N.H. (2020) The potential use of operational radar network data to evaluate the representation of convective storms in NWP models. *Quarterly Journal of the Royal Meteorological Society*, 146(730), 2315–2331. https://doi.org/10.1002/qj.3793.

Stevens, B., Feingold, G., Cotton, W. and Walko, R. (1996) Elements of the microphysical structure of numerically simulated nonprecipitating stratocumulus. *Journal of the Atmospheric Sciences*, 53(7), 980–1006. https://doi.org/10.1175/1520-0469(1996)053<0980:EOTMSO>2.0.CO;2.

Stevens, R.G., Loewe, K., Dearden, C., Dimitrelos, A., Possner, A., Eirund, G.K., Raatikainen, T., Hill, A.A., Shipway, B.J., Wilkinson, J., Romakkaniemi, S., Tonttila, J., Laaksonen, A., Korhonen, H., Connolly, P., Lohmann, U., Hoose, C., Ekman, A.M.L., Carslaw, K.S. and Field, P.R. (2018) A model intercomparison of ccn-limited tenuous clouds in the high arctic. *Atmospheric Chemistry and Physics*, 18(15), 11041–11071. https://doi.org/10.5194/acp-18-11041-2018.

Tang, Y., Lean, H.W. and Bornemann, J. (2013) The benefits of the met office variable resolution nwp model for forecasting convection. *Meteorological Applications*, 20(4), 417–426. https://doi.org/10.1002/met.1300.

Taufour, M., Vié, B., Augros, C., Boudevillain, B., Delanoë, J., Delautier, G., Ducrocq, V., Lac, C., Pinty, J.-P. and Schwarzenböck, A. (2018) Evaluation of the two-moment scheme lima based on microphysical observations from the hymex campaign. *Quarterly Journal of the Royal Meteorological Society*, 144(714, A), 1398–1414. https://doi.org/10.1002/qj.3283.

Thompson, G. and Eidhammer, T. (2014) A study of aerosol impacts on clouds and precipitation development in a large winter cyclone. *Journal of the Atmospheric Sciences*, 71(10), 3636–3658. https://doi.org/10.1175/JAS-D-13-0305.1.

Tobo, Y., Prenni, A.J., DeMott, P.J., Huffman, J.A., McCluskey, C.S., Tian, G., Pöhlker, C., Pöschl, U. and Kreidenweis, S.M. (2013) Biological aerosol particles as a key determinant of ice nuclei populations in a forest ecosystem. *Journal of Geophysical Research-Atmospheres*, 118(17), 10100–10110. https://doi.org/10.1002/jgrd.50801.

Van Weverberg, K., Morcrette, C.J., Boutle, I., Furtado, K. and Field, P.R. (2021) A bimodal diagnostic cloud fraction parameterization. Part I: motivating analysis and scheme description. *Monthly Weather Review*, 149(3), 841–857. https://doi.org/10.1175/MWR-D-20-0224.1.

Vie, B., Pinty, J.P., Berthet, S. and Leriche, M. (2016) Lima (v1.0): a quasi two-moment microphysical scheme driven by a multimodal population of cloud condensation and ice freezing nuclei. *Geoscientific Model Development*, 9(2), 567–586. https://doi.org/10.5194/gmd-9-567-2016.

Vogel, B., Vogel, H., Baeumer, D., Bangert, M., Lundgren, K., Rinke, R. and Stanelle, T. (2009) The comprehensive model system COSMO-ART - Radiative impact of aerosol on the state of the atmosphere on the regional scale. *Atmospheric Chemistry and Physics*, 9(22), 8661–8680. https://doi.org/10.5194/acp-9-8661-2009.

Walters, D., Baran, A.J., Boutle, I., Brooks, M., Earnshaw, P., Edwards, J., Furtado, K., Hill, P., Lock, A., Manners, J., Morcrette, C., Mulcahy, J., Sanchez, C., Smith, C., Stratton, R., Tennant, W.,

Tomassini, L., Van Weverberg, K., Vosper, S., Willett, M., Browse, J., Bushell, A., Carslaw, K., Dalvi, M., Essery, R., Gedney, N., Hardiman, S., Johnson, B., Johnson, C., Jones, A., Jones, C., Mann, G., Milton, S., Rumbold, H., Sellar, A., Ujiie, M., Whitall, M., Williams, K. and Zerroukat, M. (2019) The met office unified model global atmosphere 7.0/7.1 and JULES global land 7.0 configurations. *Geoscientific Model Development*, 12(5), 1909–1963. https://doi.org/10.5194/gmd-12-1909-2019.

Westbrook, C., Ball, R., Field, P. and Heymsfield, A. (2004) Universality in snowflake aggregation. *Geophysical Research Letters*, 31(15), L15104. https://doi.org/10.1029/2004GL020363.

Wilkinson, J.M., Porson, A.N.F., Bornemann, F.J., Weeks, M., Field, P.R. and Lock, A.P. (2013) Improved microphysical parametrization of drizzle and fog for operational forecasting using the met office unified model. *Quarterly Journal of the Royal Meteorological Society*, 139(671), 488–500. https://doi.org/10.1002/qj.1975.

Wilson, D. and Ballard, S. (1999) A microphysically based precipitation scheme for the UK meteorological office unified model. *Quarterly Journal of the Royal Meteorological Society*, 125(557), 1607–1636. https://doi.org/10.1002/qj.49712555707.

Wilson, D.R., Bushell, A.C., Kerr-Munslow, A.M., Price, J.D. and Morcrette, C.J. (2008) PC2: a prognostic cloud fraction and condensation scheme. I: scheme description. *Quarterly Journal of the Royal Meteorological Society*, 134(637), 2093–2107. https://doi.org/10.1002/qj.333.

Wood, N., Staniforth, A., White, A., Allen, T., Diamantakis, M., Gross, M., Melvin, T., Smith, C., Vosper, S., Zerroukat, M. and Thuburn, J. (2014) An inherently mass-conserving semi-implicit semi-Lagrangian discretization of the deep-atmosphere global non-hydrostatic equations. *Quarterly Journal of the Royal Meteorological Society*, 140(682), 1505–1520. https://doi.org/10.1002/qj.2235.

Yuter, S. and Houze, R. (1995) 3-dimensional kinematic and microphysical evolution of florida cumulonimbus.2. Frequency-distributions of vertical velocity, reflectivity, and differential reflectivity. *Monthly Weather Review*, 123(7), 1941–1963. https://doi.org/10.1175/1520-0493(1995)123<1941:TDKAME>2.0.CO;2.

How to cite this article: Field, P.R., Hill, A., Shipway, B., Furtado, K., Wilkinson, J., Miltenberger, A. *et al*. (2023) Implementation of a double moment cloud microphysics scheme in the UK met office regional numerical weather prediction model. *Quarterly Journal of the Royal Meteorological Society*, 149(752), 703–739. Available from: https://doi.org/10.1002/qj.4414

APPENDIX A. CASIM IMPLEMENTATION IN THE UNIFIED MODEL

In this appendix the process rates for the double-moment implementation of CASIM will be briefly introduced. In addition, the changes to the CASIM scheme relative to its MONC implementation for coupling with the UM will be described. This description is appropriate for the model version and suites presented in this article. Some processes follow or have been adapted from those described in the Met Office Large Eddy Model documentation (Gray *et al.*, 2001).

A.1. CASIM formulation

CASIM has five hydrometeor species: cloud liquid, rain, cloud ice, snow, and graupel. A generalised gamma distribution for all species is

$$\mathcal{N}(D) = n_x \frac{\lambda_x^{1+\mu_x}}{\Gamma(1+\mu_x)} D^{\mu_x} \exp(-\lambda D), \tag{A1}$$

where D is the particle size, $\mathcal{N}(D)$ is the PSD, n_x is the number concentration for that species (x = cloud liquid, rain, cloud ice, snow, or graupel), λ_x is the slope parameter that evolves as mass and number change, and μ_x is a shape parameter that is fixed for this UM implementation. To simplify some of the equations that follow it is convenient to define the intercept parameters:

$$n_{0x} = n_x \frac{\lambda_x^{1+\mu_x}}{\Gamma(1+\mu_x)}. \tag{A2}$$

In this work we present the double-moment configuration of CASIM, in which μ_x is prescribed. CASIM can be configured to represent three moments for rain, snow, and graupel, where μ_x is diagnosed from a combination of three prognostic moments (mass, number, and a third moment). See Shipway and Hill (2012) for a more complete description. At the time of writing, cloud liquid and cloud ice in CASIM can be used in single- or double-moment configuration. In the following, mass (q) and number (n) mixing ratio have units of kg· kg^{-1} and kg^{-1} respectively, and SI units are used unless stated otherwise. The subscript letters w, r, i, s, and g for q and n represent cloud liquid, rain, cloud ice, snow, and graupel species respectively.

A.2. Parameter settings

Parameters describing the properties of the different hydrometeor species and relevant references are given in Table A1.

A.3. CASIM prognostic equations

In this section we will define the warm, mixed-phase and cold prognostic double-moment transfer equations in CASIM, which are applied in the UM. For traceability of equations back to the CASIM, where appropriate, we relate the equations to the CASIM modules, to aid with understanding of the code and equations. All the code module references are correct for CASIM vn1.0.0.

TABLE A1 CASIM hydrometeor parameters

	Terminal fall speed[a]				Mass–dimension[b]			Shape parameter	
Species	***a***	***b***	***f***	**Note**	***c***	***d***	**Note**	**mu**	**Note**
Cloud	3×10^7	2	0.5	Stokes sphere	522	3	Liquid sphere	2.5	
Rain	a_1=4854, a_2=-446	b1=1.0, b2=0.782	0.5	Abel and Shipway 2007, g1=0,g2=4085.35	522	3	Liquid sphere	2.5	
Ice	6×10^6	2	0.5	Stokes sphere	$200\pi/6$	3	Sphere	2.5	
Snow	12	0.5	0.5		0.026	2	Cotton *et al.*, 2013	2	Field *et al.*, 2007
Graupel	253	0.734	0.422		$500\ \pi/6$	3		2.5	

[a] $v = aD^b(\rho_0/\rho)^f$, SI units, D is particle maximum span and ρ_0 is the reference density of air (1.22 kg m^{-3}). For Abel and Shipway rain $v=[a_1 D^{b1} e^{(-g1D)}+a_2 D^{b2} e^{(-g2D)}](\rho 0/\rho)^f$

[b] $m = cD^d$, SI units.

Table A2 presents the subscripts for all the CASIM process rates that impact mass mixing ratio and number concentration. Where a similar process impacts multiple hydrometeors, a consistent naming convention is applied. For example, dep is vapour deposition, sed is sedimentation, mlt is melting, and ac refers to accretion, where the collector hydrometeor appears first in the description and the captured hydrometeor is last. We acknowledge that accretion can also be referred to as capture and, in the context of mixed-phase interactions, riming.

$$
\begin{aligned}
\frac{Dq_\mathrm{v}}{Dt} &= P_\mathrm{isub} + P_\mathrm{ssub} + P_\mathrm{gsub} + P_\mathrm{revp} \\
&\quad - P_\mathrm{condensation} - P_\mathrm{idep} - P_\mathrm{sdep} - P_\mathrm{gdep} \\
\frac{Dq_\mathrm{w}}{Dt} &= P_\mathrm{sedw} + P_\mathrm{condensation} - P_\mathrm{raut} - P_\mathrm{racw} - P_\mathrm{iacw} \\
&\quad - P_\mathrm{sacw} - P_\mathrm{gacw} - P_\mathrm{homc} - P_\mathrm{inuc} \\
\frac{Dn_\mathrm{w}}{Dt} &= N_\mathrm{sedw} + N_\mathrm{activation} - N_\mathrm{waut} - N_\mathrm{racw} \\
&\quad - N_\mathrm{iacw} - N_\mathrm{sacw} - N_\mathrm{gacw} - N_\mathrm{homc} - N_\mathrm{inuc} \\
\frac{Dq_\mathrm{i}}{Dt} &= P_\mathrm{sedi} + P_\mathrm{inuc} + P_\mathrm{homc} + P_\mathrm{iacw} + P_\mathrm{idep} \\
&\quad + P_\mathrm{ihal} - P_\mathrm{raci} - P_\mathrm{saci} - P_\mathrm{gaci} - P_\mathrm{saut} \\
&\quad - P_\mathrm{isub} - P_\mathrm{imlt} \\
\frac{Dn_\mathrm{i}}{Dt} &= N_\mathrm{sedi} + N_\mathrm{inuc} + N_\mathrm{homc} + N_\mathrm{ihal} - N_\mathrm{raci} \\
&\quad - N_\mathrm{saci} - N_\mathrm{gaci} - N_\mathrm{iaut} - N_\mathrm{isub} - N_\mathrm{imlt} \\
\frac{Dq_\mathrm{r}}{Dt} &= P_\mathrm{sedr} + P_\mathrm{raut} + P_\mathrm{racw} + P_\mathrm{raci} \\
&\quad + P_\mathrm{smlt} + P_\mathrm{gmlt} - P_\mathrm{revp} - P_\mathrm{sacr} - P_\mathrm{gacr} \\
&\quad - P_\mathrm{homr} \\
\frac{Dn_\mathrm{r}}{Dt} &= N_\mathrm{sedr} + N_\mathrm{raut} + N_\mathrm{gshd} + N_\mathrm{smlt} + N_\mathrm{gmlt} \\
&\quad - N_\mathrm{revp} - N_\mathrm{sacr} - N_\mathrm{gacr} - N_\mathrm{homr} - N_\mathrm{racr} \\
\frac{Dq_\mathrm{s}}{Dt} &= P_\mathrm{seds} + P_\mathrm{saut} + P_\mathrm{saci} + P^{\#}{}_\mathrm{raci} + P_\mathrm{sacr} + P_\mathrm{sacw} \\
&\quad + P_\mathrm{sdep} - P_\mathrm{gacs} - P_\mathrm{smlt} - P_\mathrm{ssub} - P_\mathrm{ihal} \\
\frac{Dn_\mathrm{s}}{Dt} &= N_\mathrm{seds} + N_\mathrm{saut} + N^{\#}{}_\mathrm{raci} - N_\mathrm{gacs} \\
&\quad - N_\mathrm{smlt} - N_\mathrm{ssub} - N_\mathrm{sacs} \\
\frac{Dq_\mathrm{g}}{Dt} &= P_\mathrm{sedg} + P_\mathrm{gacs} + P_\mathrm{gacw} + P_\mathrm{gaci} + P_\mathrm{gacr} + P^{\#}{}_\mathrm{raci} \\
&\quad - P_\mathrm{gmlt} + P_\mathrm{homr} + P_\mathrm{sacw}(=0) \\
&\quad + P_\mathrm{sacr}(=0) - P_\mathrm{gsub} + P_\mathrm{gdep} \\
\frac{Dn_\mathrm{g}}{Dt} &= N_\mathrm{sedg} + N_\mathrm{homr} + N_\mathrm{sacw}(=0) + N_\mathrm{sacr}(=0) + N^{\#}{}_\mathrm{raci}
\end{aligned}
\tag{A3}
$$

Processes prefixed with P are mass mixing ratio rates and N are number concentration rates; the subscripts v, w, r, i, s, and g represent water vapour, cloud liquid, rain, cloud ice, snow and graupel species respectively. The # superscript indicates that the source term depends on a threshold to control whether it is applied to graupel or snow (A.5.2).

A.4. Autoconversion

In a bulk cloud microphysics scheme, where liquid and ice phases are split into smaller cloud and larger rain or snow species, autoconversion represents the self-collection of the "cloud" species to form particles that populate the rain or snow species.

A.4.1. Liquid cloud to rain

In this work, autoconversion of liquid cloud to rain is parametrised following Khairoutdinov and Kogan (2000) with mass tendency

$$
P_\mathrm{raut} = 1350 q_\mathrm{w}^{2.47} \left(\frac{n_\mathrm{w}\rho}{10^6} \right)^{-1.79} \tag{A4}
$$

TABLE A2 CASIM process rate subscript description for each process related to the hydrometeors

Subscript	Description
gacs	Graupel–snow accretion rate
gacw	Graupel–cloud water accretion rate
gdep	Deposition rate for graupel
gmlt	Graupel melting rate
gshd	Graupel shedding of rain rate
gsub	Graupel evaporation (sublimation) rate
homc	Homogeneous nucleation rate of cloud
homr	Homogeneous freezing of rain
iacw	Ice-water accretion rate; that is, riming rate of ice crystals
idep	Deposition rate of ice crystals
imlt	Melting rate of ice crystals
inuc	Heterogeneous nucleation rate
isub	Evaporation (sublimation) of ice crystals
racw	Rain–cloud water accretion rate
raut	Rain autoconversion rate
revp	Rain evaporation rate
saci	Snow–ice accretion rate
sacr	Snow–rain accretion rate
sacw	Snow–cloud water accretion rate; that is, riming rate of snow aggregates
saut	Snow autoconversion rate (from ice crystals)
sdep	Deposition rate of snow aggregates
sedg	Graupel sedimentation rate
sedi	Ice crystal sedimentation rate
sedl	Cloud liquid sedimentation rate
sedr	Rain sedimentation rate
seds	Snow aggregate sedimentation rate
smlt	Melting rate of snow aggregates
ssub	Evaporation (sublimation) of snow aggregates.
condensation	Condensation/evaporation rate from the Unified Model cloud-fraction scheme
activation	Droplet number rate from activation

Note: The subscript initial letters w, r, i, s, and g represent cloud liquid, rain, cloud ice, snow, and graupel species respectively.

and number tendency

$$N_{\text{raut}} = \frac{P_{\text{raut}}}{c_{\text{r}} \frac{\mu_{\text{aut}}}{3.0} D_{0\text{aut}}^3}, \tag{A5}$$

where c_{r} is defined in Table A1, $D_{0\text{aut}}$ is the diameter at which drizzle drops are produced in Khairoutdinov and Kogan (2000) (defined as $r_0 = 25$ μm therein) and μ_{aut} is a diagnostic evaluation of the cloud shape parameter based on the parametrisation from Martin *et al.* (1994). The sink of cloud droplet number converting to rain is

$$N_{\text{waut}} = \frac{P_{\text{raut}} n_{\text{w}}}{q_{\text{w}}}. \tag{A6}$$

In addition to Khairoutdinov and Kogan (2000), CASIM also includes Kogan (2013), which uses a similar form but with different constants that are more appropriate for cumulus clouds.

The CASIM module for warm rain autoconversion is src/autoconversion.F90.

TABLE A3 Values of collection efficiencies E_{xy} with species x collecting species y

Collection efficiency	Value	Routine	Reference
E_{iw}	0	src/ice_accretion.F90	
E_{sw}	0.5	src/ice_accretion.F90	Following snow riming in Furtado and Field (2017)
E_{gw}	1.0	src/ice_accretion.F90	
E_{sr}	1	src/ice_accretion.F90	
E_{gr}	Inactive		
E_{ri}	1	src/ice_accretion.F90	
E_{si}	$0.2e^{0.08T_c}$	src/ice_accretion.F90	
E_{gi}	$0.2e^{0.08T_c}$	src/ice_accretion.F90	
E_{gs}	$0.2e^{0.08T_c}$	src/ice_accretion.F90	
E_{ss}	$0.1e^{0.08T_c}$	src/aggregation.F90	
E_{rr}	1.0	src/aggregation.F90	Beheng (1994)
E_{ii}	Inactive		
E_{gg}	Inactive		

Note: T_c is the temperature in Celsius.

A.4.2. Ice crystals to snow

Autoconversion of ice to snow particles is carried out as follows:

$$P_{saut} = \begin{cases} \frac{q_i}{\tau_{saut}} \left[\left(\frac{\lambda_{i,min}}{\lambda_i} \right)^{d_i} - 1 \right], & \text{if } \lambda_i < \lambda_{i,min} \\ 0, & \text{otherwise.} \end{cases} \quad \text{(A7)}$$

where d_i is defined in Table A1 and the the minimum slope of the ice size distribution is $\lambda_{i,min} = (1 + d_i + \mu_i)/D_{i,max}$, where $D_{i,max} = 100$ μm.

The number concentration tendency for this process is based on assuming that newly formed snow particles have a size $D_{i,s} = 50$ μm:

$$N_{saut} = \frac{P_{saut}}{(c_i D_{i,s}^{d_i})}, \quad \text{(A8)}$$

where c_i is defined in Table A1

The sink of cloud ice number converting to snow is

$$N_{iaut} = \frac{P_{saut} n_i}{q_i}. \quad \text{(A9)}$$

The transfer of cloud ice to snow is an even bigger uncertainty than the autoconversion of cloud water to rain. For liquid this transfer is mainly through accretion. For ice it can be through aggregation, diffusion, or, most likely, a combination of both. Though collision/collection kernels are empirically defined for liquid droplets, there are none for ice. By making the threshold small (i.e., $D_{i,s} = 50$ μm), the conversion from cloud ice to snow will be dominated by diffusional growth, which is better characterised for these small particles relative to aggregation.

The CASIM module for autoconversion of ice to snow is src/snow_autoconversion.F90.

A.5. Collection processes

Collection processes in CASIM, and this work, are generically defined as the rate at which particles with different fall speeds will collide and stick together. Collection processes are processes such as accretion and aggregation and are based on simple gravitational sweepout arguments combined with an efficiency of the collision occurring and leading to a sticking or coalescence event given the imposed gravitational collection kernel. In CASIM, we defined accretion processes as a collection process between two hydrometeor types (e.g., rain collecting cloud water), which impacts both mass mixing ratio and number concentration of both hydrometeor types. In contrast, we define aggregation as being self-collection of one hydrometeor type, which results in a change in number concentration but no change in mass mixing ratio. All the collection processes are dependent on the parametrisation of the collection efficiency, and these are provided in Table A3, along with the CASIM module.

A.5.1. Accretion of cloud water by rain

The mass tendency for cloud water is based on the approach of Khairoutdinov and Kogan (2000):

$$P_{racw} = 67(q_w q_r)^{1.15}, \quad \text{(A10)}$$

where q_w and q_r are the mass mixing ratio of cloud water and rain.

The number tendency for cloud water is

$$N_{racw} = P_{racw}\frac{q_w}{n_w}, \tag{A11}$$

where n_w is number concentration of cloud water. Accretion of cloud water by rain results in reduction (increase) in cloud mass (rain mass) and a decrease in cloud number concentration but no change in rain number concentration.

As with the autoconversion, CASIM also includes Kogan (2013), which uses a similar form to Khairoutdinov and Kogan (2000) but different parameters.

The CASIM module for accretion of cloud water by rain is src/accretion.F90.

A.5.2. Mixed-phase and cold-phase collection between particles of different hydrometeors

The collection process in CASIM is represented either as a binary process, based on a binary collection equation, for species that can exhibit relatively large fall speeds (1 m $\cdot$ s^{-1}) or a simple gravitational sweepout for combinations of collector hydrometeors (x) and the collected species (y), which have relatively small fall speed; that is, when $y = \mathrm{i}, \mathrm{w}$.

The simpler sweepout process is given as

$$P_{xacy} = \frac{\pi n_x a_x \Gamma(3 + b_x + \mu_x) E_{xy} q_y}{4(\lambda_x)^{3+b_x+\mu_x}} \left(\frac{\rho_0}{\rho}\right)^{g_x}, \tag{A12}$$

where n_x is the number concentration mixing ratio of the collector hydrometeor x, q_y is the mass mixing ratio of the species being collected, E_{xy} is the collection efficiency (Table A3), a_x, b_x, μ_x, and g_x are the parameters for the collector hydrometeor x as defined in Table A1, and $\rho_0 = 1.22$ kg$\cdot$ m^{-3} is a reference value of air density.

For collisions where the fall speeds of both species cannot be assumed to be small, the binary collection equation controls the rate at which hydrometeor x collects hydrometeor y, which results in an increase (decrease) in the mass of hydrometeor x (y). This collection is given as follows:

$$P_{xacy} \approx c_y \delta E_{xy} \left[\frac{\Gamma(1 + \mu_y + d_y)}{\lambda_y^{1+\mu_y+d_y}} \frac{\Gamma(3 + \mu_x)}{\lambda_x^{3+\mu_x}} + 2\frac{\Gamma(2 + \mu_y + d_y)}{\lambda_y^{2+\mu_y+d_y}} \frac{\Gamma(2 + \mu_x)}{\lambda_x^{2+\mu_x}} + \frac{\Gamma(3 + \mu_y + d_y)}{\lambda_y^{3+\mu_y+d_y}} \frac{\Gamma(1 + \mu_x)}{\lambda_x^{1+\mu_x}} \right], \tag{A13}$$

where $\delta E_{xy} = \pi n_{0x} n_{0y} E_{xy} \delta V_{xy}/4\rho$, and where δV_{xy} is the larger of the difference in mass-weighted fall speeds and a quarter of the fastest falling particle:

$$\delta V_{xy} = \max\left(\frac{\max(V_x, V_y)}{4}, |V_x - V_y|\right). \tag{A14}$$

For the number concentration tendency, a similar approach is employed:

$$N_{xacy} \equiv N_{yacx} = \delta E_{xy} \left[\frac{\Gamma(1 + \mu_y)}{\lambda_y^{1+\mu_y}} \frac{\Gamma(3 + \mu_x)}{\lambda_x^{3+\mu_x}} + 2\frac{\Gamma(2 + \mu_y)}{\lambda_y^{2+\mu_y}} \frac{\Gamma(2 + \mu_x)}{\lambda_x^{2+\mu_x}} + \frac{\Gamma(3 + \mu_y)}{\lambda_y^{3+\mu_y}} \frac{\Gamma(1 + \mu_x)}{\lambda_x^{1+\mu_x}} \right].$$

Binary collection of mixed phase can also result in the production of a third hydrometeor species z. Snow collecting water and forming graupel was found to generate too much graupel in the troposphere above 10 km in tropical simulations and led to a large unrealistic reduction in cirrus cloud cover. Therefore, it is disabled pending reassessment of the process rates related to this. Currently in CASIM, the production of a z through binary collection only occurs for rain collecting ice and converting to graupel. For this to occur the amount of rain collecting ice needs to be larger than 10^{-4} kg$\cdot$ kg^{-1} and has the following formulation:

$$P_{xyz} = P_{xacy} + P_{yacx} \tag{A15}$$

$$N_{xyz} = N_{xacy}, \tag{A16}$$

where P, N_{xyz} is the change in the mass and number mixing ratio when a third hydrometeor is formed from binary collection.

The main CASIM module for accretion of mixed- and cold-phase hydrometeors is src/ice_accretion.F90. Depending on the input arguments, this routine uses the functions within the modules src/sweepout_rate.F90 and src/binary_collection.F90 to derive the process rates.

A.5.3. Self-collection processes

Self-collection processes, which are defined as aggregation processes in CASIM, represent the process rate for the collection within a hydrometeor type. This type of collection will only impact the number concentration and will have no impact on the mass of the hydrometeor type.

The main CASIM module for aggregation is src/aggregation.F90.

Rain collecting rain. The approach of Beheng (1994) is used to represent the rain self-collection

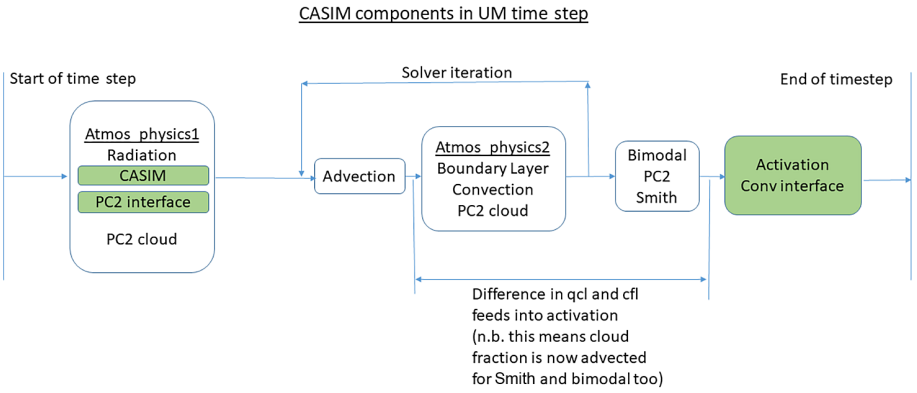

FIGURE A1 Schematic of Unified Model time step indicating in green boxes where CASIM-related changes are made [Colour figure can be viewed at wileyonlinelibrary.com]

number tendency:

$$N_{\text{racr}} = -8E_{\text{rr}} n_{\text{r}} q_{\text{r}} \rho, \tag{A17}$$

where E_{rr} is the collection efficiency, n_{r} and q_{r} are the number and mass mixing ratios respectively, and the constant has units $\text{m}^3 \cdot \text{kg}^{-1}$.

Snow collecting snow. Following the implementation of double-moment snow in the Met Office Large Eddy Model (Gray *et al.*, 2001), the number concentration tendency is

$$N_{\text{sacs}} = a_{\text{s}} (\rho_0/\rho)^{g_{\text{s}}} n_{0\text{s}}^2 E_{\text{ss}} \lambda_{\text{s}}^{-h_{\text{s}}} I(\mu_{\text{s}}, b_{\text{s}}), \tag{A18}$$

where $h_{\text{s}} = 4 + 2\mu_{\text{s}} + b_{\text{s}}$ and $I = \pi \int \int (j+k)^2 \, |j^{\text{b}} - k^{\text{b}}| \, j^a k^a \, \text{e}^{-(j+k)} \, dj \, dk$.

Ice collecting ice (IACI) and graupel collecting graupel (GACG) are done in exactly the same way but are inactive in the UM implementation.

A.6. Phase changes

A.6.1. Vapour diffusional growth of cloud and cloud fraction in the UM

When CASIM is used in the MONC large-eddy simulation model (Dearden *et al.*, 2018) and KiD (Shipway and Hill, 2012; Hill *et al.*, 2015; Miltenberger *et al.*, 2020) the condensation of moisture to form droplets is done using an "all-or-nothing" saturation adjustment scheme in CASIM, which means clouds are either on or off within a grid box; that is, cloud fraction of 1 or 0. In the UM, however, a cloud fraction scheme is used to represent the impact of subgrid humidity variations and the formation of fractional cloud occurrence through saturation adjustment. Such a scheme is required to support the seamless philosophy of the UM. In this section, we describe the technical coupling of the CASIM to the cloud fraction scheme in the UM.

The nature of the time step for the semi-Lagrangian advection Wood *et al.*, (2014) approach employed in the UM is such that the condensation of liquid is performed by the cloud scheme at a different point in the time step relative to the microphysics. This differs from the CASIM condensation calculation in MONC and/or KiD, in which condensation is done at the same point in the time step as the rest of the microphysics. Therefore, to interface double-moment CASIM with the UM cloud fraction schemes, the activation of aerosol to form cloud droplets has been separated from CASIM and carried out towards the end of the UM time step following condensation.

For background, the UM simplified time-step structure is shown schematically in Figure A1. There are two Atmospheric Physics calls separated by the advection step. Within Atmospheric Physics 1 the radiation and cloud physics are carried out both using the same start of time-step values. The semi-Lagrangian advection scheme uses an iterative step around Atmospheric Physics 2 to compute the departure points, and it is this iterative step that dictates which parametrisations sit in Atmospheric Physics 2: the boundary layer and convection scheme. As already mentioned, because, in the UM, CASIM is coupled to the UM cloud schemes, the condensation and activation step is disabled in CASIM, when CASIM is used in the UM (this does not occur in MONC or KiD). Then, activation is carried out after the advection and Atmospheric Physics 2 components have been completed and all the condensation increments of Atmospheric Physics 2 have completed.

The UM currently has three cloud schemes available. The first is a simple diagnostic cloud scheme (Smith, 1990), the second a prognostic cloud scheme (Wilson *et al.*, 2008), and the third is a turbulent kinetic energy based diagnostic scheme that accounts for mixing across strong thermodynamic and moisture boundaries (bimodal scheme; Van Weverberg *et al.*, 2021). At the time of writing, the diagnostic Smith and bimodal cloud scheme are used in regional configurations only, whereas PC2 is employed in Global NWP and early tropical regional configurations. Coupling to CASIM is provided for all of these cloud schemes, but only bimodal is presented in this article (see Figure A1 for the main coupling features of CASIM in the UM time step).

TABLE A4 CASIM hydrometeor fraction diagnosis

Hydrometeor	Diagnosis
CASIM liquid cloud fraction	UM liquid cloud fraction
CASIM ice cloud fraction	UM frozen cloud fraction
CASIM snow fraction	UM frozen cloud fraction
CASIM rain fraction	MAX(CASIM fraction liquid, CASIM fraction rain from level above)
CASIM graupel fraction	CASIM fraction rain (has no effect if graupel is not present)

Note: All microphysical process rates use "in-cloud" values. Therefore, in-cloud values are found by dividing the grid-box mean value by its respective fraction or mixed-phase fraction for mixed-phase processes. UM: Unified Model.

Although PC2 is the only prognostic cloud fraction scheme in the UM, the liquid, frozen, and bulk cloud fractions are still advected for the diagnostic bimodal schemes when CASIM is active. This is so that a change in cloud fraction due to condensation can be diagnosed and prevent in-cloud droplet concentrations increasing if cloud fraction decreases. If the cloud fraction reduces, then the grid-box mean droplet number is also reduced so that the in-cloud droplet number remains constant. This represents an inhomogeneous mixing:

$$\Delta n_{\mathrm{w}} = \frac{\Delta C_{\mathrm{l}}}{C_{\mathrm{l}}} n_{\mathrm{w}}. \tag{A19}$$

The cloud fraction values are passed into CASIM and five hydrometeor fractions are diagnosed and used to generate in-cloud masses and numbers for the microphysical process rates. The rain fraction on the lowest model level is passed out of casim_ctl for use in the land scheme: Jules (Best *et al.*, 2011).

The fractions are diagnosed in the manner described in Table A4.

For model grid boxes where both ice and liquid phases are present it is necessary to make an assumption about the volume fraction overlap. If there is no overlap then mixed-phase processes will be zero. If the overlap is assumed to be maximum then so too will be the mixed-phase process rates. In the CASIM implementation in the UM this assumption is defined by the mixed-phase overlap factor mpof. This factor scales the overlap from minimum (mpof = 0) to maximum (mpof = 1). This factor has the potential to strongly modulate mixed-phase process rates and is important for the evolution of mixed-phase cloud longevity, precipitation, and albedo. The overlap mixed-phase fraction, O_{lf} that is used to scale the microphysical process rates is found by combining the frozen and liquid hydrometeor fractions with mpof:

$$\begin{aligned} O_{\mathrm{lf}} = {} & \max(0.0, \mathrm{mpof} \times \min(C_{\mathrm{f}}, C_{\mathrm{l}}) \\ & + \max(0, (1 - \mathrm{mpof})(C_{\mathrm{f}} + C_{\mathrm{l}} - 1)). \end{aligned} \tag{A20}$$

In the simulations presented here mpof = 0.5. Note that if mpof = 0 that $O_{\mathrm{lf}} = C_{\mathrm{l}}$ if $C_{\mathrm{f}} = 1$.

A.6.2. Activation

The previous section describes the use of a cloud fraction and how this affects microphysical process rates. When CASIM is double moment, as in this article, and cloud water is formed through condensation, a calculation is then carried out to provide a droplet number concentration. When using the prescribed number option (as in CASIM-2M), the grid-box mean droplet number is set to the fixed value multiplied by liquid cloud fraction.

With the option to use aerosol to derive cloud droplet number concentration, CASIM uses the Gordon *et al.* (2020) methodology to derive maximum supersaturation and cloud drop number concentration. Gordon *et al.* (2020) is an adaptation of the Abdul-Razzak and Ghan (2000) approach to account for pre-existing cloud droplets and competition for water vapour. Briefly, the scheme initially assumes that aerosols and not droplets dominate the sink of water vapour and that the sink due to droplets is negligible. This calculation is then repeated assuming that droplets dominate the sink of water vapour and the sink due to aerosols is negligible. The lower of the two calculated maximum supersaturations is then used to activate additional aerosols. On time steps when cloud fraction increases in a partially cloudy grid box, the "old cloud", where the sink of water vapour is dominated by droplets, and the "new cloud", where the sink is dominated by aerosols, are distinguished and new droplets from each part of the cloud are calculated separately before being weighted by the relevant cloud fraction and summed. For 1.5 km simulations the velocity used to derive the maximum supersaturation is the explicitly resolved value, but a factor multiplied by the subgrid turbulent kinetic energy (tke) can also be used to compute the vertical velocity for activation: $w_{\mathrm{act}} = w + c\sqrt{\mathrm{tke}}$, where c is a constant and w is the explicitly resolved vertical velocity. For the ARCL and MURK tests here, $c = 0$.

The module responsible for CASIM activation in the UM uses the evaporation or condensation that occurs across Atmospheric Physics 2 and calls the CASIM activation scheme. This generates increments in droplet number, mass, and aerosol number and mass. Following Stevens *et al.* (1996), and others, the increment in droplet number concentration may only be positive unless the cloud fraction in the grid cell decreases; in other words, if the cloud fraction does not change during a time step then the new droplet concentration only replaces the old droplet concentration if the new droplet concentration exceeds the old. If the cloud fraction in the grid cell decreases, the droplet concentration is reduced proportionately.

In the UM, aerosols can be represented by user-defined free tracers, UKCA (United Kingdom Chemistry and Aerosols)-mode, MURK, or climatologies (e.g., ARCL). Droplet activation can occur based on aerosol information from those aerosol fields and environmental conditions. UKCA-mode is a full prognostic two-moment aerosol microphysics scheme that is based on GLOMAP-mode (Mann *et al.*, 2010) and used in climate configurations (Mulcahy *et al.*, 2021). UKCA-mode provides both aerosol mass and number information for the activation of droplets.The approach by Gordon *et al.* (2020) is used to reduces the in-cloud activation of aerosol due to vapour competition effects. At present, the fully prognostic aerosol scheme is too expensive for NWP applications, and so this scheme was not used in this work. Gordon *et al.* (2020) presents the details of the coupling of UKCA-mode to CASIM and results using configuration close to the RA1M version (Bush *et al.*, 2020). Here, we describe the coupling of MURK and ARCL climatologies to CASIM.

A.7. Coupling to MURK

MURK is a simple single-moment prognostic aerosol used in the UKV regional model. MURK mass mixing ratio, humidity, and visibility are combined in the data assimilation process to provide improved visibility and humidity. The WB microphysics used simple relations to map from aerosol mass to cloud droplet number concentration (Wilkinson *et al.*, 2013). For a simple coupling to MURK the mass combined with a nominal log-normal ammonium sulphate PSD with assumed mode size 9.5×10^{-8} m, geometric standard deviation 1.4, and density 1,769 kg $\cdot$ m^{-3} is used to diagnose a number concentration. This accummulation mode population of aerosol (assuming hygroscopicity, $B_k = 0.4$) is then used in the activation scheme to produce a droplet number concentration within the range 1×10^6 to 250×10^6 kg^{-1}. The droplet number then can feed through to the microphysical process rates.

A.8. Coupling to ARCL aerosol climatology

In regions where MURK is not available the aerosol climatology (Bellouin *et al.*, 2011) can be used. Currently, this is a mass-only monthly varying climatology of soluble and insoluble aerosol species. To use with CASIM, the soluble species are summed and assumed to be represented by ammonium sulphate particles and treated in the same way as for MURK.

A.8.1. Evaporation, sublimation, deposition – general

In CASIM, diffusional growth or loss of all hydrometeors other than cloud is based the electrostatic analogue approach and used to calculate the sensible heat transfer to or from a rain hydrometeor or cold-phase hydrometeors by conduction and convection from the surrounding air. For all hydrometeors (rain, ice, snow, and graupel), this growth or loss process can be described as follows:

$$P_{\text{evap}} = \int n(D) \frac{(q_{\text{v}}/q_{\text{sat}} - 1)}{\text{AB}} CF(D)\, dD, \tag{A21}$$

where subscript evap can be replaced with *x*sub or *x*dep, depending on temperature and hydrometeor type, q_{sat} can be either saturation mixing ratio with respect to liquid or ice, again depending on temperature and hydrometeor type, and AB is a function of temperature and depends on the phase change in question:

$$\text{AB} = \frac{L^2}{K_{\text{a}} R_{\text{v}} T^2} + \frac{1}{\rho q_{\text{sat}} \psi}, \tag{A22}$$

where L is the latent heat of the phase change and ψ is the diffusivity of water vapour in air, K_{a} is the thermal conductivity of air, R_{v} is gas constant for water vapour and T is temperature.

In Equation (A21) the factor C is the shape parameter or "capacitance" (for spherical particles $C = 2\pi D$) and F is the ventilation coefficient for particles falling through water vapour; that is:

$$F = 0.78 + 0.31 S_{\text{c}}^{1/3} R_{\text{e}}^{1/2}, \tag{A23}$$

where $R_{\text{e}} = V(D)D\rho/\upsilon$ is the Reynolds number, υ is the kinematic viscosity of air, and S_{c} is the Schmidt number (the ratio of υ to ψ).

The integrated ventilation factor includes the capacitance, ventilation coefficient, and size distribution, $\mathcal{V}_x =$

$\int 2\pi DF\mathcal{N}_x(D)\,dD$, is

$$\mathcal{V}_x = 2\pi\mathcal{N}_x\rho\left[0.78\frac{(1+\mu_x)}{\lambda_x} + 0.31\left(\frac{a_x\rho}{\upsilon}\right)^{1/2} S_c^{1/3}\left(\frac{\rho_0}{\rho}\right)^{1/4} \times \frac{\Gamma(0.5b_x+\mu_x+2.5)}{\Gamma(1+\mu_x)} \times\left(1+\frac{0.5f_x}{\lambda_x}\right)^{-(0.5b_x+\mu_x+2.5)} \lambda_x^{(-0.5b_x-1.5)}\right], \quad \text{(A24)}$$

where x can stand for r, i, s, or g.

A.8.2. Evaporation of rain

As described already, the evaporation and condensation of cloud water is handled in the cloud fraction scheme of the UM. Since this is based on a saturation adjustment scheme, the air is never supersaturated, and therefore condensation of water vapour onto rain does not occur. However, when rain falls into a subsaturated air, then it will start to evaporate as defined in the following:

$$P_{\text{revp}} = \frac{\left(\frac{q_v}{q_{\text{wsat}}} - 1\right)}{\rho \text{AB}_{\text{liq}}} \times \mathcal{V}_r, \quad \text{(A25)}$$

where q_v is water vapour, q_{wsat} is saturation vapour mixing ratio with respect to water, and $\mathcal{V}_r$ is the ventilation coefficient (Equation (A24) for rain) and AB_{liq} is the thermodynamic term for liquid drops and is given by

$$\text{AB}_{\text{liq}} = \frac{L_v^2}{K_a R_v T^2} + \frac{1}{\rho q_{\text{wsat}}\psi}, \quad \text{(A26)}$$

where q_{wsat} is the saturation vapour mixing ratio with respect to liquid and L_v is the latent heat of vaporisation. If the inhomogeneous assumption for evaporation is made, which is the default assumption, then evaporation of rain maintains mean size and reduces the rain number concentration as

$$N_{\text{revp}} = P_{\text{revp}}\frac{n_r}{q_r}. \quad \text{(A27)}$$

In CASIM, the homogeneous assumption can be made for rain evaporation, and under this assumption $N_{\text{revp}} = 0$; that is, rain evaporation does not impact rain number concentration until all of the rain water is evaporated and then all rain number is also removed.

In CASIM, the main module that controls rain evaporation is src/evaporation.F90.

A.8.3. Sublimation and deposition

Ice particles grow by vapour deposition when the air is supersaturated with respect to ice. The rate of change of mass of an ice particle due to vapour deposition or sublimation is similar to the evaporation equation.

By integrating over all particle sizes, the deposition/-sublimation growth rates of cloud ice, snow, or graupel ($P_{x\text{dep}}$ / $P_{x\text{sub}}$) can be given by

$$P_{x\text{dep}}\ (\text{or}\ -P_{x\text{sub}}) = \frac{\left(\frac{q_v}{q_{\text{isat}}} - 1\right)}{\rho \text{AB}_{\text{ice}}} \times \mathcal{V}_x. \quad \text{(A28)}$$

$\mathcal{V}_x$ is the ventilation coefficient for the x species, where x is ice, snow, or graupel (see Equation (A24)), and AB_{ice} is the thermodynamic term for ice and is given by

$$\text{AB} = \frac{L_s^2}{K_a R_v T^2} + \frac{1}{\rho q_{\text{isat}}\psi}, \quad \text{(A29)}$$

where q_{isat} is the saturation vapour mixing ratio with respect to ice and L_s is the latent heat of sublimation. When snow and graupel particles are undergoing sublimation the number concentration is assumed to decrease at a rate of - $P_{x\text{sub}} \times n_x/q_x$, where x is s or g respectively. There is no source of particles when ice undergoes deposition.

In CASIM, the main module that controls deposition of vapour and sublimation is src/ice_deposition.F90.

A.8.4. Melting

The melting of cloud ice, graupel, and snow acts as a source of rain. The melting of cloud ice is assumed to be instantaneous:

$$P_{\text{imlt}} = \frac{q_i}{\Delta t}, \quad \text{(A30)}$$

where Δt is the model timestep. The melting rates of snow or graupel melted are calculated using thermal heat balance considerations:

$$P_{\text{smlt}} = \frac{\mathcal{V}_s}{\rho L_f}[K_a T_c + L_v\psi\rho(q_v - q_{\text{isat}})] + \frac{c_w T_c}{L_f}(P_{\text{sacw}} + P_{\text{sacr}}), \quad \text{(A31)}$$

$$P_{\text{gmlt}} = \frac{\mathcal{V}_g}{\rho L_f}[K_a T_c + L_v\psi\rho(q_v - q_{\text{isat}})] + \frac{c_w T_c}{L_f}(P_{\text{gacw}} + P_{\text{gacr}} - P_{\text{gshd}}), \quad \text{(A32)}$$

where L_f is the latent heat of fusion, c_w the specific heat of liquid water and T_c is the temperature in Celsius. The

number concentration rates from snow or graupel to rain due to these processes are assumed to be

$$N_{\mathrm{smlt}} = P_{\mathrm{smlt}} \frac{n_{\mathrm{s}}}{q_{\mathrm{s}}} \tag{A33}$$

and

$$N_{\mathrm{gmlt}} = P_{\mathrm{gmlt}} \frac{n_{\mathrm{g}}}{q_{\mathrm{g}}} \tag{A34}$$

respectively.

In CASIM, the module that controls melting process rates is src/ice_melting.F90.

A.9. Primary production of ice

In CASIM, initial production of ice occurs through heterogeneous ice nucleation or homogeneous freezing of cloud and/or rain.

A.9.1. Heterogenous ice nucleation

When not using aerosol to act as ice nucleating particles, the default approach for ice heterogeneous freezing is to nudge the cloud ice number concentration to the value suggested by Cooper (1987) as a function of temperature, as long as the grid box is at water saturation and the temperature is below −8°C.

Using aerosol to act as ice nucleating particles, a number of heterogeneous freezing parametrisations become available. These work by linking the dust concentrations (available through tracers or UKCA-mode) to changes in ice crystal number through heterogeneous ice nucleation. The parametrisations of DeMott *et al.* (2010), Niemand *et al.* (2012), Atkinson *et al.* (2013), Tobo *et al.* (2013), and DeMott *et al.* (2015) are available (Miltenberger *et al.*, 2020).

In CASIM, the module that controls melting process rates is src/ice_nucleation.F90.

A.9.2. Heterogeneous rain freezing

Immersion freezing of raindrops to form graupel is based on Bigg (1953), who showed that the probability of a raindrop freezing per unit time is

$$(\pi/6) D^3 B_{\mathrm{B}} (\mathrm{e}^{-A_{\mathrm{B}} T_{\mathrm{c}}} - 1), \tag{A35}$$

where A_{B} and B_{B} are parameters determined from laboratory experiment.

The rates of conversion of rain mass and number to graupel are as follows:

$$P_{\mathrm{homr}} = n_{0\mathrm{r}} \frac{\pi B_{\mathrm{B}}}{6\rho} c_{\mathrm{r}} (\mathrm{e}^{-A_{\mathrm{B}} T_{\mathrm{c}}} - 1) \frac{\Gamma(4 + d_{\mathrm{r}} + \mu_{\mathrm{r}})}{\lambda_{\mathrm{r}}^{4+d_{\mathrm{r}}+\mu_{\mathrm{r}}}}$$
$$N_{\mathrm{homr}} = n_{0\mathrm{r}} \frac{\pi B_{\mathrm{B}}}{6\rho} (\mathrm{e}^{-A_{\mathrm{B}} T_{\mathrm{c}}} - 1) \frac{\Gamma(4 + \mu_{\mathrm{r}})}{\lambda_{\mathrm{r}}^{4+\mu_{\mathrm{r}}}}, \tag{A36}$$

where μ_{r} and d_{r} are defined in Table A1

In CASIM, the module that controls melting process rates is src/homogeneous_freezing.F90.

A.9.3. Homogeneous freezing of water

If the temperatures is below the homogeneous freezing temperature threshold (−38°C) and cloud water mass exceeds 10^{-9} kg· kg^{-1} then the liquid water will be frozen. The number of droplets frozen can either be set to freeze all available droplets ($\mathrm{ni}_{\mathrm{limit}}$) or use the environmental conditions to estimate the number frozen that would quench the supersaturation for air subject to an upward vertical velocity. This is done by assuming droplets freeze and form ice spheres with, $\mathrm{D}_{0\mathrm{hom}}$, 50 μm diameter. Thereafter, by balancing the Squires equation for supersaturation, the change in number concentration of ice spheres for a given updraft speed and environmental conditions can be found. This value is used as the number concentration of droplets lost and cloud ice particles produced. This approach avoids problems where high number concentrations ($> 10^7$ m^{-3}) of cloud ice are formed and then persist at cirrus altitudes.

$$N_{\mathrm{homc}} = \frac{w_{up} a_{\mathrm{w}}}{B_{\mathrm{i}} D_{0\,\mathrm{hom}} \Delta t}, \tag{A38}$$

where $w_{up} = MAX(w, 0)$, Δt is the timestep and

$$a_{\mathrm{w}} = \frac{g L_{\mathrm{v}} R_{\mathrm{d}}}{R_{\mathrm{d}} T c_p R_{\mathrm{v}} T} - 1.$$

$$B_{\mathrm{i}} = b_{\mathrm{m}} B_0 \left(\frac{E_{\mathrm{w}}}{E_{\mathrm{i}}} - 1 \right),$$

$$b_{\mathrm{m}} = \frac{1}{q_{\mathrm{v}}} + \frac{L_{\mathrm{v}} L_{\mathrm{f}}}{c_p R_{\mathrm{v}} T^2},$$

$$B_0 = 4\pi A_{\mathrm{i}} \frac{\rho_i}{\rho_{\mathrm{a}}},$$

and

$$\frac{1}{A_{\mathrm{i}}} = \frac{\rho_{\mathrm{i}} L_{\mathrm{f}}^2}{k_{\mathrm{a}} R_{\mathrm{v}} T^2} + \frac{\rho_{\mathrm{i}} R_{\mathrm{v}} T}{E_{\mathrm{i}} D_{\mathrm{v}}}.$$

where g is acceleration due to gravity, cp is the specific heat capacity of air at constant pressure, E_{w}, E_{i} are the saturation vapour pressures for liquid and ice, and ρ_{i} is the density of ice. In CASIM, the module that controls melting process rates is src/homogeneous_freezing.F90.

A.10. Secondary ice production

At present, only one secondary production process is currently implemented in CASIM: the ice splinter production through riming known as the Hallett–Mossop effect.

The rates of water droplet accretion by graupel and snow are used to compute the number and mass of ice splinters produced.

The rates are modulated by a triangular function between between −2.5°C and −7.5°C, that peaks at −5°C. It is assumed that 350 ice splinters are formed for 10^{-6} kg of rimed liquid at −5°C and each splinter (M_{I0}) has a mass of 10^{-18} kg (Hallet and Mossop 1974), so

$$P_{\text{ihal}} = 3.5 \times 10^{8} M_{I0}(P_{\text{gacw}} + P_{\text{sacw}}) f(T), \tag{A39}$$

where $f(T) = 1$ at −5°C and falls off linearly to zero as temperature is increased to −2.5°C and or decreased to −7.5°C.

In CASIM, the module that controls melting process rates is src/homogeneous_freezing.F90.

A.11. Graupel specific processes

Graupel can form from rain accreting ice (see accretion). Graupel growing by the collection of other water species can sometimes accrete more liquid than can be frozen due to latent heating bringing the surface of the graupel to the melting temperature. Any unfrozen liquid is shed and added to the rain category. This is known as wet growth. If liquid accretion is not rapid enough to cause wet growth then the graupel undergoes dry growth.

Dry growth is assumed if

$$P_{\text{gacr}} + P_{\text{gacw}} < P_{\text{gwet}} \tag{A40}$$

or the temperature is colder than the homogeneous freezing temperature. P_{gwet} is the threshold amount of liquid that the graupel can freeze before shedding occurs and is based on Musil (1970):

$$P_{\text{gwet}} = \left(\frac{910}{\rho_{\text{g}}}\right)^{0.625} \frac{\rho L_{\text{v}} D_{\text{v}}(q_{0\text{sat}} - q_{\text{v}}) - K_{\text{a}} T_{\text{c}}}{\rho(L_f + c_{\text{w}} T_{\text{c}})} \mathcal{V}_{\text{g}} + (P^{\text{wet}}_{\text{gaci}} + P^{\text{wet}}_{\text{gacs}}) \left(1 - \frac{c_{\text{i}} T_{\text{c}}}{L_{\text{f}} + c_{\text{w}} T_{\text{c}}}\right), \tag{A41}$$

where $q_{0\text{sat}}$ is the saturation mixing ratio with respect to liquid water at 0°C, $\mathcal{V}_{\text{g}}$ is the ventilation coefficient for graupel, c_{w} and c_{i} are the specific heat capacities of liquid and ice respectively, K_{a} is the thermal conductivity of air, D_{v} the diffusivity of air, and L_{v} and L_{f} are the latent heats of vapourisation and fusion respectively. The factor of $(910/\rho_{\text{g}})^{0.625}$ was adopted from the Met Office Large Eddy Model.

If the graupel is undergoing wet growth then P_{gacr} is recalculated to account for unfrozen liquid being shed as rain:

$$P_{\text{gacr}} = P_{\text{gwet}} - P_{\text{gacw}} - P_{\text{gaci}} - P_{\text{gacs}}; \tag{A42}$$

if P_{gacr} is negative then

$$P_{\text{gshd}} = \min\{P_{\text{gacw}}, -P_{\text{gacr}}\}. \tag{A43}$$

The number concentration of graupel does not change when graupel collects water from the other categories. The number concentrations of the collected categories are reduced as described in ice accretion. Note that dry growth collection of ice and snow is disabled, but if they were included the mass and number collection rates would be recalculated according to a linear efficiency factor.

In CASIM, the module that controls melting process rates is src/graupel_wetgrowth.F90.

A.11.1. Snow to graupel

The formation of new graupel from riming of snow follows the formulation of Reisner *et al.* (1998):

$$P_{\text{gsacw}} = \frac{3\pi\alpha(\rho_{\text{a}} q_{\text{w}} a_{\text{s}} \text{Eff})^2 n_{\text{s}}.\Gamma(\mu+1)\Gamma(2b_{\text{s}}+2)}{4(\rho_{\text{g}} - \rho_{\text{s}})\lambda^{2b_{\text{s}}+1-\mu}}, \tag{A44}$$

and then the number of newly formed graupel is diagnosed as

$$N_{gsacw} = \max\left(\frac{\rho_s P_{\text{gsacw}}}{(\rho_{\text{g}} - \rho_{\text{s}})\rho_{\text{a}} m_{\text{g0}}}, 0\right), \tag{A45}$$

where m_{g0} is the mass of a graupel embyro and ρ_{s},ρ_{g} are the assumed densities for snow and graupel. However, this process is currently disabled in this UM implementation.

In CASIM, the module that controls melting process rates is src/graupel_embryos.F90.

A.12. Sedimentation

The equation for the terminal velocity is given by the following

$$V_x(D) = a_x D^{b_x} \, e^{f_x D} \left(\frac{\rho_0}{\rho}\right)^{g_x}, \tag{A46}$$

where a_x, b_x, f_x, and g_x represent the parameters for the fall speed relationship as defined in Table A1.

The semi-Lagrangian dynamical core allows the UM to use relatively large time steps (e.g., 60 s for 1 km horizontal grid resolution). Because of narrowing of level spacing in the vertical near to the surface this would mean that hydrometeors could cross several grid levels unless substepping of the microphysics or sedimentation were carried out. To avoid this, the approach taken already in the UM (Wilson and Ballard, 1999) is based on the solution suggested by Rotstayn (1997). The increment for mass mixing ratio q_x or number mixing ratio (replace q_x by n_x)

due to flux divergence as hydrometeors fall is

$$P_{\text{sedx}} = \frac{R_{\text{f}}}{\rho \Delta z} - q_x \frac{\overline{V_x}}{\Delta z}, \tag{A47}$$

which when integrated analytically gives

$$q_x(t + \Delta t) = q_x(t)[\exp(-\alpha)] + \frac{R_{\text{f}} \Delta t}{\rho \Delta z}[1 - \exp(-\alpha)], \tag{A48}$$

where $\alpha = \overline{V_x} \Delta t / \Delta z$ is the Courant number, $\overline{V_x}$ is the mean mass-weighted or number-weighted fall speed, depending on whether mass or number is being sedimented, and Δt and Δz are the time step and layer thickness respectively. R_{f} is the flux from above ($\rho q_x V_x$ or $\rho n_x V_x$ from the layer above). This approach of using an exponential filter when Courant numbers are large provides stability for the model.

A.13. Size distribution limiting

For model stability, to stop size distributions becoming too narrow or too broad each hydrometeor has a threshold large and small mean size. If the mean size exceeds the large threshold or is smaller than the minimum threshold then the λ parameter is linearly scaled to set it to the threshold value. Then the other parameters of the distribution are recomputed. The thresholds are widely spaced and are rarely, if ever, crossed during a typical forecast.